2012

ATR-FTIR STUDIES ON THE KINETICS OF DIMETHYLARSINIC ACID (DMA) SURFACE COMPLEXATION WITH IRON(OXYHYDR)OXIDES

Julia Tofan-Lazar Miss
Wilfrid Laurier University, tofa0190@wlu.ca

ATR-FTIR STUDIES ON THE KINETICS OF

DIMETHYLARSINIC ACID (DMA) SURFACE

COMPLEXATION WITH IRON(OXYHYDR)OXIDES

Julia Tofan-Lazar

Honours Bachelor of Science, Wilfrid Laurier University, 2010

THESIS

Submitted to the Department of Chemistry

in partial fulfillment of the requirements for

Master of Science

Wilfrid Laurier University

2012

List of Publications:

1) Tofan-Lazar, J.; Al-Abadleh H.A., ATR-FTIR Studies on the Adsorption/Desorption Kinetics of Dimethylarsinic Acid on Iron-(oxyhydr)oxides. *J.Phys.Chem.A* 116 (2012) 1596-1604

2) Tofan-Lazar, J.; Al-Abadleh H.A., Fast Kinetic ATR-FTIR Studies on Phosphate Adsorption on Iron-(oxyhydr)oxides in the Absence and Presence of Surface Arsenic: Molecular-level Insights into the Ligand Exchange Mechanism. Manuscript accepted by *J.Phys.Chem. A*, September 25, 2012

Abstract:

Dimethylarsinic acid (DMA) is an organoarsenical compound that, along with monomethylarsonic acid, poses a health and an environmental risk, and a challenge to the energy industry. Little is known about the surface chemistry of DMA at the molecular level with materials relevant to geochemical environments and industrial sectors. The surface chemistry of phosphorus and arsenic compounds in their organic and inorganic forms is of great interest due to its role in controlling their transport, bioaccessibility and speciation. This thesis reports the first *in-situ* and surface-sensitive rapid kinetic studies on the adsorption and desorption of DMA to and from Fe-(oxyhydr)oxide films hematite and goethite at pH 7 and I=0.01 M KCl using attenuated total reflection Fourier transform infrared spectrometry (ATR-FTIR). The adsorption of phosphate in the presence and absence of DMA and arsenate was also carried out. Values for the apparent rates of adsorption and desorption of DMA were extracted from experimental data as a function of spectral components, flow rate of the aqueous phase, film thickness of hematite, and using chloride and hydrogen phosphate as desorbing agents.

The DMA adsorption kinetic data showed fast and slow rates, consistent with the formation of more than one type of adsorbed DMA complex. Apparent pseudo adsorption and pseudo desorption rate constants were extracted from the dependency of the initial adsorption rates on [DMA(aq)]. Desorption rate constants were also extracted from desorption experiments using hydrogen phosphate and chloride solutions, and were found to be higher by 1- 2 orders of magnitude than those using chloride.

The phosphate adsorption kinetic data showed adsorption rate constants of phosphate on Fe-(oxyhydr)oxide films increase in this order: arsenate-covered < DMA-

covered ≤ freshly-prepared. Also, desorption rate constants of DMA complexes were 7 times higher than arsenate using phosphate as a desorbing agent. When these results are combined with earlier work on the thermodynamics, kinetics, and structure of surface complexes, this data suggests that, within minutes to 1 hr of surface interaction, increasing organic substitution on arsenate increases the proportion of relatively weakly-bonded complexes (ie. monodentate and outer-sphere).

Table of Contents:

List of Figures:

List of Tables:

1 Introduction:

1.1 Arsenic in the Environment

Arsenic is element 33 in the periodic table, the 20th most abundant trace metalloid in the earth's crust, and can be found in environmental systems all around the world in crystalline, powder, amorphous, or vitreous forms. Atmospheric concentrations range from 0.5ng/m^3 to 2.8ng/m^3 and occur mostly as particulates of oxides and sulfides from industrial emissions mainly from copper smelting, coal combustion, and municipal incineration (1). Biological processes contribute approximately 0.2 to 26x10^6 kg/year to that amount (1).

Surface soils that humans are most likely to come into contact with contain variable amounts of arsenic which are usually found bound up as arsenate to iron and manganese oxy(hydroxy)oxides and is not readily mobile or bioavailable. Concentrations vary based on the amount of organic matter present in the soils giving a global average of about 5 ppm (1). However, the global range is quite variable with areas like the US having arsenic levels of 7.5 ppm while areas such as lower Austria have arsenic levels varying from 100-115 ppm (1). Anthropogenic influence can result in localised arsenic concentrations ranging from 250 ppm to 10000 ppm and in certain areas, even greater (1).

Arsenic levels in rivers and lakes are about 0.1 to 1.7 µg/L (1). However some groundwater can have concentrations in the mg/L range (1). Depending on the geological location of these bodies of water, the levels will once again vary (2). Seawater has a natural concentration of 1 to 4 µg/L with an estimated median value of 3.7 µg/L (1). This arsenic exists mostly as the inorganic, biologically accessible species, arsenate and

arsenite. In water rich in sulphur, sulphur can displace oxygen from these species so that thioarsenates and thioarsenites become the predominant arsenicals (1). Some methylarsenic species are encountered, usually in lower concentrations where there is biological activity such as algal growth (1).

Due to the ubiquitous presence of arsenic in our environment, animals and plants cannot escape exposure to this element and have learned to cope in order to survive (2). The worm *Lumbricus rubellus* lives in the polluted soil of what was once the site of the 19th century Devon Great Consols mine in Tavistock, UK (1). The mine used to be the world's largest source of arsenic resulting in surrounding soils having concentrations reaching 9800 ppm (1). Another worm from the marine environment, *Tharyx marioni,* is capable of accumulating arsenic up to a concentration of 13000 ppm, while the fern *Pteris vitata* accumulates inorganic arsenic up to a concentration of 23000 ppm (1).

1.1.1 Inorganic Arsenic

Arsenic occurs naturally in over 200 different mineral forms of which 60% are arsenates, 20% sulfides and sulfosalts and the remaining 20% includes arsenides, arsenites, oxides, silicates and elemental arsenic (As) (3). Inorganic forms of arsenic (iAs), most commonly found in the environment, occur at the oxidation states +3 As(III) and +5 As(V). Under aerobic conditions, arsenate, As(V), is the dominant species allowing stronger binding to soil leading to little mobility, while under reducing conditions, arsenite, As(III), is the dominant species which is more soluble and therefore more mobile in the environment (3). Redox potential (Eh) and pH are the most important factors governing inorganic arsenic speciation (4). The pKa's of H_3AsO_4 are: 2.22, 6.98,

and 11.53 while the pKa's of H_3AsO_3 are 9.2, 12.1, and 13.4 (5). Therefore, under

oxidizing conditions and pH less than 6.9, $H_2AsO_4^-$ is the dominant species, whereas at

higher pH, $HAsO_4^{2-}$ is the dominant species (3). H_3AsO_4 and AsO_4^{3-} may be present in

extremely acidic and basic conditions, respectively (3). Under reducing conditions where

the pH is less than 9.2, the uncharged arsenite species, H_3AsO_3, predominates.

At low pH and high concentrations of reduced sulfur, dissolved As(III) sulfide

species can be formed rapidly by reduction of arsenate by H_2S (3). Reducing, acidic, and

sulfur-rich conditions also favor precipitation of orpiment (As_2S_3), realgar (AsS), or other

arsenic sulfide minerals (3). In more alkaline environments, As(III) sulfides are more

soluble and higher dissolved arsenic concentrations are possible (3). Weathering of

minerals such as pyrite and scorodite will release their contained arsenic into the

environment and different environmental conditions will lead to different arsenic species.

Rainfall will then transport these into ground and surface waters.

1.1.2 Organic Arsenic

Organic arsenic species are important in food, particularly sea-food, and are only

a minor component of total arsenic in natural waters (3). Complex organic arsenic

compounds such as tetramethylarsonium salts, arsenocholine, arsenobetaine,

dimethyl(ribosyl)arsine oxides and arsenic containing lipids are identified in the marine

environment and only a minor fraction of total arsenic in oceans remains in solution, as

the majority is sorbed on to suspended particulate materials (2). Organic arsenic

concentrations are greatest in organic-rich waters such as soil, sediment pore waters and

productive lake water but very low in ground waters (3). The concentrations of organic

3

species are increased by methylation reactions catalyzed by microbial activity, including

bacteria, yeasts, and algae (3). The most common forms of organic arsenic found in the

environment are dimethylarsinic acid (DMA) and monomethylarsonic acid (MMA) (6).

What makes these arsenic compounds organic is that they contain both carbon and

hydrogen. During summer when microbial activity increases and close to the sediment

water interface organic arsenic species become more abundant (3). While the

concentrations of organic arsenic species are low in most natural environments, the

methylated and dimethylated As(III) species are of considerable interest since they have

been found to be more cytotoxic, more genotoxic, and more potent enzyme inhibitors

than inorganic As(III) (3). The most common organic arsenic compounds found in the

environment are shown in Table 1.

Table 1. Organic arsenic compounds commonly found in the environment (Adapted from
Reference 1).

Compound Name	Compound Structure
Monomethylarsonic Acid (MMA)	
Dimethylarsinic Acid (DMA)	
Arsenobetaine	
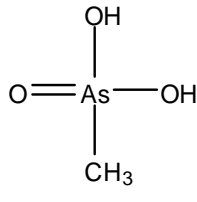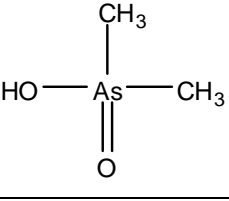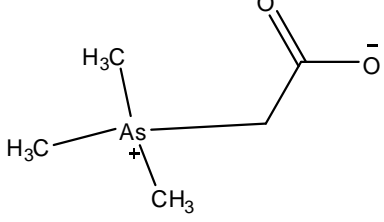
Table 1. Continued.

Compound Name	Compound Structure
Tetramethylarsonium ion	H_3C—As^+—CH_3 with CH_3 above and CH_3 below
Trimethylarsine Oxide	H_3C—As=O with CH_3 above and CH_3 below
Methylarsine	H_2As—CH_3
Dimethylarsine	H_3C $\overset{H}{As}$ CH_3
Trimethylarsine	H_3C, H_3C bonded to As—CH_3
Arsenosugars	(ring structure with R, OH, OH, O, and H_3C—As=O—CH_3)

R = (various substituent structures shown)

1.1.3 Arsenic Cycling Pathways: Redox and Methylation Chemistry

Methylated organoarsenicals such as MMA and DMA are produced in biomethylation processes of inorganic arsenic that occur under anaerobic conditions in the presence of microbes in organic rich sediments (7). The two main pathways that explain biomethylation of As are the Challenger mechanism (7), and the Hayakawa pathway (8), which involve multioxidative methylation and reduction steps. In the Challenger mechanism, DMA forms as an intermediate, whereas it is found to be a final biomethylation product in the Hayakawa pathway.

To proceed from arsenate to trimethylarsine, four two-electron reductions are required and shown in Figure 1 as the Challenger mechanism. Each reduction produces a compound with an electron lone pair on the arsenic atom; with the exception of the final step (7). Each reduction product is then methylated by any methyl donor present in biological systems such as arsenic methyltransferase (Cyt 19), reduced glutathione (GSH), or S-adenosyl-$_L$-methionine (SAM) (7).

To convert arsenate to trimethylarsine, the reductions are likely to be enzyme catalyzed with reducing agents providing the necessary $2e^-$. The reductants are believed to be thiols with particular attention being given to glutathione (GSH) and lipoic acid (6,8-dithiooctanoic acid) (7). There is little experimental evidence from microbial systems and the mechanism is complicated by the ability of arsenic compounds to react with thiols, but it is assumed that the reactions resemble those for formation of methylarsonate and dimethylarsinate in mammals (7).
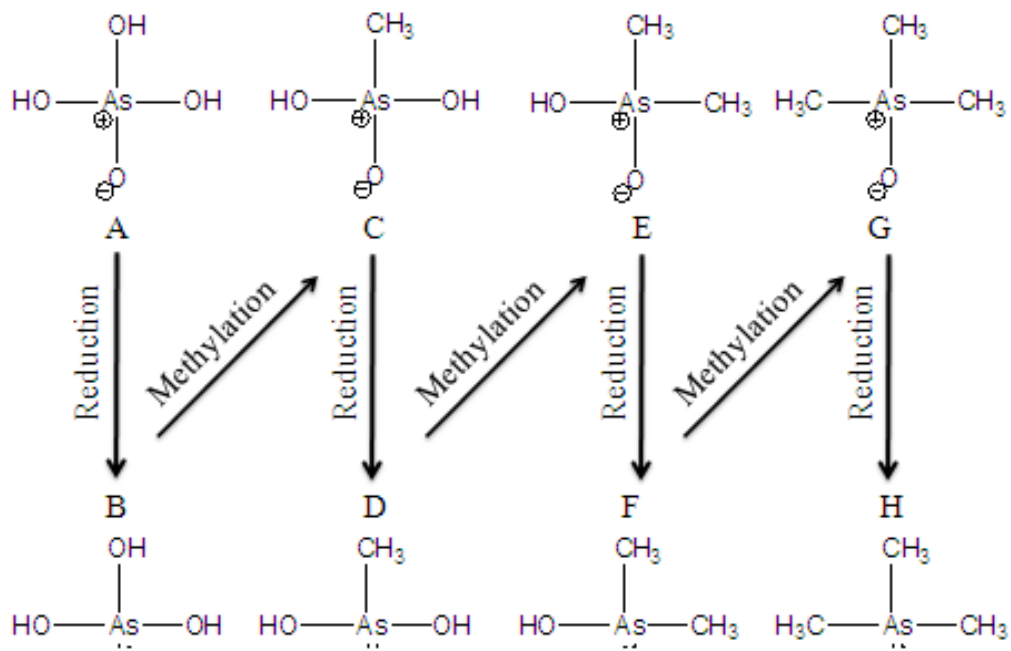
Figure 1. Challenger mechanism for the conversion of arsenate to trimethylarsine. (A) Arsenate; (B) Arsenite; (C) Methylarsonate; (D) Methylarsonite; (E) Dimethylarsinate; (F) Dimethylarsinite; (G) Trimethylarsine oxide; (H) Trimethylarsine (Adapted from Bentley and Chaateen, reference 7).

While the Challenger mechanism sees the pentavalent metabolites being reduced to the more toxic trivalent compounds, a more unconventional metabolic pathway is the Hayakawa pathway which sees the trivalent metabolites being converted to the less toxic pentavalent compound (8). This new pathway is in accordance with the concept that oxidation reactions lead to detoxification of arsenic. As shown in Figure 2, both arsenic triglutathione (ATG) and monomethylarsenic diglutathione (MADG) are substrates for human Cyt19 for further methylation to dimethylarsinic glutathione (DMAG) (8). Arsenite is metabolized and converted to DMA by Cyt19 via formation of As-GSH complexes rather than via repetitive reduction and oxidative methylation (8).

7
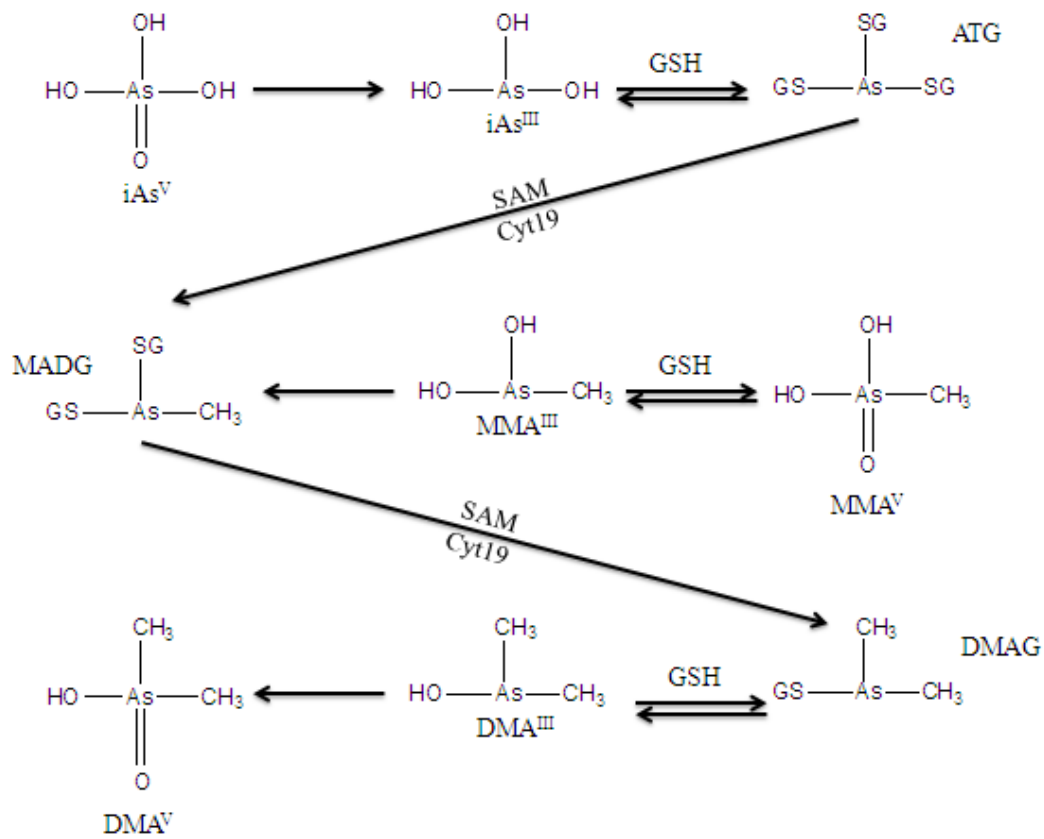
Figure 2. The Hayakawa pathway (Adapted from Hayakawa *et al.*, reference 8).

The Challenger and Hayakawa pathways show overall reactions that may occur in the environment, but the different microbial processes involved in arsenic biochemistry are shown in Figure 3. Arsenate enters the cell through phosphate transporters while arsenite enters through the aqua-glyceroporins due to the analogy of arsenic chemical species to other molecules (9). Once inside the cell, arsenate is reduced to arsenite by ArsC, which is further forced out of the cell by the specific pump ArsB (9). Arsenite can also be detoxified by complexation with Cys-rich peptides due to its affinity for thiol groups, or it can serve as an electron donor by oxidation. In this context, biological oxidation of arsenite could be a detoxification mechanism. Arsenate on the other hand

can be an electron acceptor during respiration processes and inorganic arsenic species in the cell can be transformed into organic species by methylation (9).
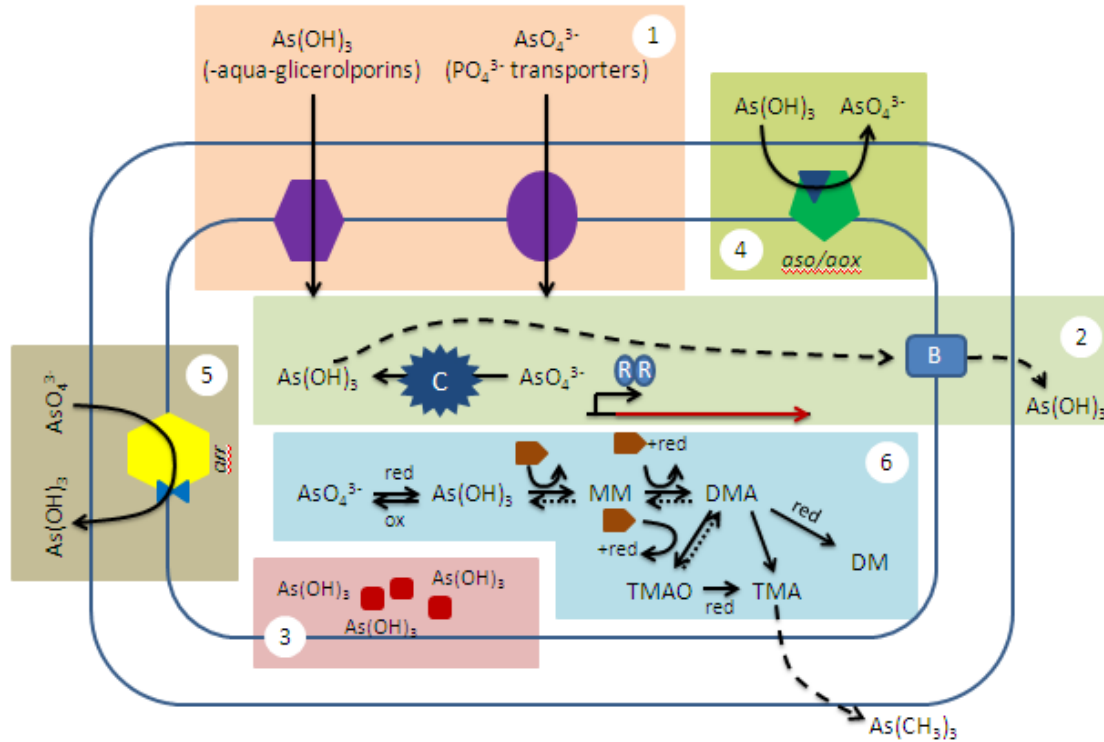
Figure 3. (1) Inorganic arsenic entering the cell (2) Reduction of arsenate by ArsC and extrusion by ArsB (3) Arsenite detoxification by complexation with Cys-rich peptides (4) Arsenite serving as an electron donor (5) Arsenate as electron acceptor (6) Methylation of inorganic arsenic; DM = dimethylarsine, DMA = dimethylarsinic acid, MM = methylarsine, TMA = trimethylarsine, TMAO = trimethylarsine oxide (Adapted from Paez-Espino *et al.*, reference 9).

The amount of arsenic that can be absorbed into the body is dependent on the size of the particles inhaled or ingested and their solubility (6). Particle size will determine how far into bodily tissues they can penetrate while solubility will determine how easily absorption into the blood stream will occur (6). The trivalent form of inorganic arsenic

passes more rapidly into tissues than the pentavalent form (10). The gut in particular, absorbs arsenic compounds from food and beverages rapidly into the blood stream. Inorganic arsenic is metabolized via two main types of reactions in the body: conversion of arsenate to arsenite, and methylation (6). Once methylation takes place, arsenic can be rapidly eliminated from the body with the urine (6). Therefore, ingested organic arsenic compounds are much less extensively metabolized and more rapidly eliminated than inorganic arsenic (10).

1.1.4 Environmental Regulations of Arsenic

Environmental sources of arsenic that may lead to exposure are: water, food, soil and air with exposure being most common by via drinking water (11). Due to arsenic being an element, it persists in the environment and does not deteriorate. Production of arsenic has greatly decreased in North America in the past several years, but imports of arsenic have steadily increased. In 1851, the Arsenic Act was passed in response to the widely publicized homicidal use of arsenic at the time (1). The act allowed for regulation of the retail trade of arsenic compounds such as adult only sales, mixing the substances with soot as well as signing a "poison book" with every purchase (1). However, no restrictions were placed on its use in industry, agriculture or medicine. Around 1860, the fear of products containing arsenic peaked with members of the public calling for the wholesale regulation of arsenic and for warnings to be placed on arsenical wallpaper, commonly used at the time, prior to sale (1). Around 1877, the use of an arsenic-adulterated baby powder caused the death of 13 children and the illness of many more (1). The publicity it received was sufficient to prompt the Medical Society of London to

investigate arsenic poisoning which lead to restrictions on the arsenic trade as well as warnings to the purchasers. The Society of Arts Manufacturers and Commerce joined the fray in 1880 but concluded that there was doubt as to whether domestic poisoning by arsenic was a significant problem due to virtual absence of hard evidence on morbidity and mortality rates associated with arsenical goods (1).

In 1901, the Kelvin Commission recommended limits for the amounts of arsenic allowed in food and drink. For liquids, the limit was 0.143 mg/L, and for solid foods, the limit was 1.43 mg/L (1). These were made official when accepted as laws in 1928 which increased the interest for arsenic in the scientific community. Studies followed which lead to even more stringent criteria to these limits and a 50 µg/L national standard being set around 1950. When Congress amended the Safe Drinking Water Act in 1996, it directed the Environmental Protection Agency (EPA) to develop a new standard for arsenic levels in the nation's drinking water as the 50 µg/L standard was not found to achieve the EPA's goal for public health protection. On January 22, 2001, the EPA reported in the Federal Register that based on the best available science, an arsenic limit of 10 µg/L would go into effect in March of that year and that water systems would have until 2006 to fully implement the standard (12). Due to these limits, the interest of arsenic in water has increased leading to environmental geochemistry experiments investigating the bioavailability of arsenic in the environment.

Most living organisms that regularly encounter arsenic have developed arsenic resistance mechanisms. Some living organisms are able to utilize arsenic in their ordinary physiology. These can use arsenic for respiration and/or as electron donors (13). Some microbes can also methylate inorganic species or demethylate their organic counterparts.

11

Such microbial activities in water and soils strongly influence the speciation and bioavailability of arsenic and therefore play an important role in its environmental cycling (14). Yeast and fungi display interesting biological responses to arsenic exposure, but bacteria have lately been considered as potential environmental bioremediation agents (14).

1.2 What is DMA?

DMA is a chemical compound made up of an arsenic atom bonded to two methyl groups, a hydroxyl group, and double bonded to an oxygen atom. Therefore, this organic arsenic compound has the chemical formula: $(CH_3)_2AsO_2H$ and the chemical structure:

$$HO-\underset{\underset{O}{\overset{\overset{CH_3}{|}}{\parallel}}{As}}-CH_3$$
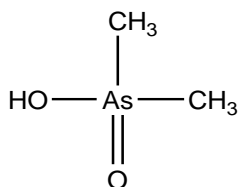
Robert Bunsen first discovered DMA or cacodylic acid when he oxidized cacodyl oxide or dimethylarsinous anhydride to produce it (1). This was a startling contribution to medicinal chemistry in finding that the hydrate of iron oxide was an antidote to arsenic poisoning which later became the underlying chemistry of arsenic removal from some drinking water technologies. DMA has one pKa value at 6.27 at which pH the protonated number of species equals that of the deprotonated species (15).

1.2.1 Natural and Anthropogenic Sources

Surface waters, oxic environments, and areas of high bacterial activity most often result in the formation of DMA following methylation of inorganic arsenic species

released due to mineral weathering (2). DMA binds less strongly to soil and is therefore more mobile in the environment leading to its transport via surface and ground water into different bodies of water. The use of water on farm lands, and for drinking by the populace, causes first hand exposure to arsenic species (2).

Arsenic, in particular para-arsanilic acid (p-AsA), has historically been used as a feed additive to promote growth of animals, protect against coccidial diseases, and improve pigmentation in broiler chickens as well as its use as a pesticide (16). p-AsA is not metabolized by the animals and will therefore be excreted in their feces. Farm lands are then fertilized using feces from different animals which exposes foods to arsenic compounds. Due to farming soils being rich in microbial activity, the cycling of arsenic to DMA and other organoarsenicals is highly possible leading to exposure to DMA through food being inescapable. The commercial use of inorganic arsenic in things like wood preservatives, alloying agents, and biocides also increases the amount of DMA due to DMA being a product of iAs biomethylation (16).

Combustion of coal and biomass grown in arsenic-rich soils or irrigated by water high in arsenic levels increases the arsenic content in fly ash (17). Upon deposition of fly ash into soil and water bodies, release and mobilization of arsenic can eventually contribute to the formation of methylated forms such as DMA depending on the biogeochemical properties of these environments (17). In addition, methylated forms of arsenic are synthesized during low temperature pyrolysis of oil shale and wood treated with chromate copper arsenate (18). Arsenicals released from refining fossil fuels and biomass grown in As-rich soils are potent catalyst poisons hindering the optimum use and conversion of these fuels (18).

Municipal solid waste is often disposed of in landfills receiving a mixture of commercial and mixed industrial wastes. Landfill leachate is generated by rainwater percolating through the landfill body mixed with water released during waste decomposition (19). This leachate can be characterized by four groups of pollutants: dissolved organic matter, inorganic macro-components, heavy metals, and xenobiotic organic compounds (19). Major potential environmental impacts generated by landfills include the pollution of ground and surface waters. Due to DMA being a by-product of arsenic's commercial uses, its concentration in the landfill body and as a result in the leachate is increased. The presence of inorganic arsenic alone may also lead to the presence of DMA as landfills are bursting with microbial activity. Therefore, whether from natural or anthropogenic sources, potential cycling of methylated organoarsenicals to the more toxic forms of arsenic, and their uptake, accumulation and transformation in plants and up the food chain is attracting considerable attention.

1.2.2 Field Measurements of DMA in Soils and Water

One field method used in the speciation of arsenic in water samples utilizes solid-phase extraction cartridges (SPE) in series for selective retention of arsenic species (20). This is followed by elution and measurement of eluted fractions by inductively coupled plasma mass spectrometry (ICP-MS) for total arsenic (20). In one study, Argentinean groundwater was found to contain 4-20% of speciated arsenic present as MMA, and 20-73% as As(III). UK surface waters were also tested, and speciated arsenic was measured as 7-49% MMA and 12-42% DMA (20).

Mestrot and co-workers developed highly sensitive, quantitative and qualitative field deployable arsenic compounds flow boxes based on silver nitrate impregnated silica gel (21). This allows low-level measurements of arsenic compounds to be made by ICP-MS coupled with high performance liquid chromatography (HPLC) for speciation (21). Arsenic efflux can be monitored using this device in both arsenic impacted and non-impacted soils and conducted through laboratory mass balances to investigate soil factors regulating emission of arsenic compounds (21). Microcosm experiments can also be carried out to determine the factors regulating As volatilization (21). From various soils tested in this study, the highest levels of arsenic species were measured in paddy soils with fluxes significantly elevated above background concentrations, and the arsenic-impacted soil having a higher flux than the non-impacted paddy (21). The arsenic flux recorded for Bangladeshi paddy soil (240 ± 90 mgha^{-1}year^{-1}) was 5-fold higher than for Spanish paddy soil (44 ± 15 mgha^{-1}year^{-1}) (21). In addition, arsenic soil porewater concentrations were 14-times higher in contaminated paddies compared to non-impacted sites with speciation analysis of the arsines from the Bangladeshi paddy soil finding trimethylarsines to be the dominant species (21). The arsines produced by the soils in the microcosms were trimethylarsines (TMAs) followed by Me_2AsH and AsH_3 (21). $MeAsH_2$ was only found in the mine impacted Chinese rice paddy tested (21).

Similar studies have been done in areas like Munich (Germany) which detected DMA at levels of $0.4 - 3.3$ μg/L, and no detectable MMA leading to organoarsenicals accounting for less than 5% of total As (22). These values were no different in organic matter rich soils and were overall considered to be of minor importance on the investigated field site (22).

Studies done on soil samples from gold-mining areas of Minas Gerais State in Brazil resulted in DMA amounts ranging from 2.2 – 28.9 µg/L (23). This was an approximate 40% of the total As detected in the samples tested (23). These samples were not expected to contain as much organoarsenicals as resulted and this was attributed to the high amount of microorganisms in the soils together with several days of incubation which made for an ideal flourishing environment, therefore leading to methylation of inorganic As to organoarsenicals such as DMA (23).

Speciation can also be carried out by pH-gradient hydride generation purge and trap gas chromatography (HG-PT-GC), followed by ICP-MS (24). One study tested samples of different soils ranging from agricultural soils to abandoned industrial soils. The highest values of DMA were found in abandoned industrial soils ranging from 0.03 – 4.36 µg/kg, followed by gardening soils ranging from 0.02 – 1.62 µg/kg, and agricultural soils ranging from 0.01 – 0.15 µg/kg (24). Other organoarsenicals such as MMA were found in higher amounts in gardening (0.16 – 11.86 µg/kg) and agricultural soils (1.11 – 6.91 µg/kg) (24). Depending on the previous processing of the soils used, the values of organoarsenicals can vary drastically. Testing agricultural soils that have been fertilized using As contaminated animal feces will increase the amount of MMA, DMA, and TMA present. When comparing these amounts to other elements present in soils, the highest amounts were detected for methylated Sb, followed by methylated As, and finally methylated Sn for agricultural, gardening and industrial soils (24).

In samples taken from forest soils, the sum of all organic As can reach 30% of the total As, but this value is much lower in mineral soils (9%). DMA was found to account for approximately 12 – 20% of that in this study (25). These seemed to result from

throughfall and litterfall and were therefore mostly found in the forest floor (25). Many more studies have been carried out to measure the amount of arsenic in different regions of the world and they have all shown the importance that must be placed on the cycling and maintaining of DMA levels below certain limits in order to ensure public safety as well as the large variation of arsenic levels all over the world (26 – 31).

1.2.3 Toxicity of DMA

The relative toxicity of an arsenical depends on whether the compound is in organic or inorganic form, the compound's oxidation state, its solubility, its physical state and purity as well as its rates of absorption and elimination (32, 33). Overall, the toxicity order of arsenic compounds in several cell lines has been found to be: DMA(III), MMA(III) > iAs(III) > iAs(V) > DMA(V), MMA(V) (34).

This order is based on carcinogenesis occurance in terms of mutational or cellular proliferation cascade models using LC_{50} values (34). Cell proliferation is an important driving force in promotion of carcinogenesis; mutation is more important in initiation and in progression in which increasing malignancy and metastatic potential develops in one cell of a large number of existing cells of intermediate malignancy (34).

The reason for DMA(III) being more toxic than MMA(III) or the toxicity of MMA(V) and DMA(V) are not well understood. DMA(V) has been shown to be more toxic than MMA(V) in 3T3 cells while MMA(V) was found to be more toxic than DMA(V) in V79 cells (35, 36). One possible mechanism for trivalent arsenicals being more toxic than their corresponding pentavalent forms is that trivalent species have higher affinity for thiol compounds and generate reactive oxygen species (36, 37).

Pentavalent arsenicals are reduced to their trivalent forms and then methylated, therefore resulting in the production of methylated pentavalent arsenicals during hepatic metabolism (38). In the serial oxidative methylation, dimethyl arsenic peroxides may be produced, which can cause oxidative stress to living systems (39). If pentavalent arsenicals are to be reduced to trivalent species before oxidation-methylation, pentavalent arsenicals may exert the toxicity equivalent to the amount of their corresponding trivalent arsenicals (41). However, in general, the toxicity of MMA(V) and DMA(V) is lower than that of MMA(III) and DMA(III) by an order of 10^{-3} to 10^{-4} (41). The higher toxicity of iAs(III) compared to iAs(V) can be explained by a faster uptake rate of iAs(III) in endothelial cells and the toxicity difference to organic arsenicals may be due to potency for induction of oxidative stress and the cellular accumulation rate of these arsenicals (41).

Certain forms of arsenic are more rapidly absorbed and therefore more toxic while others are rapidly eliminated and therefore less toxic (42). Arsenite and arsenate are highly soluble in water, and therefore pose a risk via direct ingestion. Studies on DMA in particular have concluded that it plays a role in the carcinogenesis of inorganic arsenic due to its ability to generate reactive oxygen species (43).

DMA is the major metabolite formed after exposure to tri and pentavalent inorganic arsenic via ingestion or inhalation in both humans and rodents (43). It was once thought to simply be a detoxification product of iAs, but recently accumulated evidence indicates that DMA itself has unique toxic properties (43). DMA induces an organ-specific lesion-single strand breaks in DNA, in the lungs of both mice and rats and in human lung cells in vitro (44). Mechanistic studies have suggested that this damage is

due mainly to the peroxyl radical of DMA and production of active oxygen species by pulmonary tissues (40). Multi-organ initiation-promotion studies have demonstrated that DMA acts as a promoter of urinary bladder, kidney, liver, and thyroid gland cancers in rats and as a promotor of lung tumors in mice (40). Lifetime exposure to DMA in diet or drinking water also causes a dose-dependent increase in urinary bladder tumors in rats, indicating that DMA is a complete carcinogen, and also plays a role in the carcinogenesis of inorganic arsenic (40).

1.3 Surface Chemistry of DMA

The fate of contaminants in the environment depends on their surface interactions with the different components of soil particles. The mechanism of DMA adsorption to different minerals was investigated in a number of studies using batch experiments, ex-situ synchrotron X-ray absorption, and infrared techniques. Through a recently developed method which combines X-ray scattering and spectroscopic methods, characterization of complex distribution on single crystal surfaces is possible. This technique is known as resonant anomalous X-ray reflectivity (RAXR) and it can result in structures being imaged, as in Figure 4, in a way as to give insight into surface complexation of different arsenic compounds. DMA has been shown to form inner and outer sphere complexes in mono- and bidentate configurations with iron(oxyhydr)oxides (71). The spectral features of these complexes have been identified and thermodynamic studies have quantified the surface coverage of adsorbed DMA on different iron(oxyhydr)oxides as a function of concentration and binding constants to better understand binding affinities and mechanisms (46, 47, 48).

a)   b)
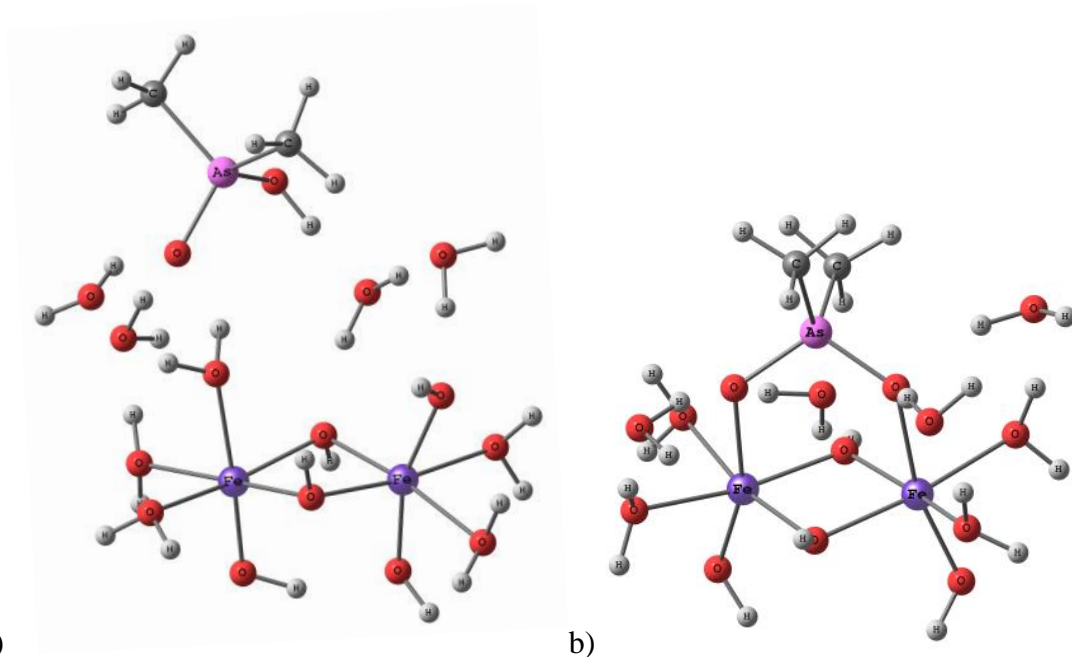
Figure 4. (a) Schematic model of outer-sphere complex formation of DMA on

iron(oxyhydr)oxide (b) Schematic model of inner-sphere complex formation of DMA on

iron(oxyhydr)oxide.

1.3.1 Adsorption/Desorption of DMA on Soils and Metal Oxides

Mobility and bioavailability of methylated organoarsenicals are controlled to a

large extent by their heterogeneous chemistry. Surface interactions of organoarsenicals

with environmental geosorbents, materials used in pollution remediation, or catalysts

employed in the petroleum industry have been the subject of a number of studies.

Materials investigated include hydrous ferric oxide and activated alumina, iron minerals

goethite, 2-line ferrihydrite, hematite, and maghemite, nanocrystalline TiO_2, amorphous

aluminum oxide, and soil (containing minerals and organic matter) (49-60). The majority

of these studies are batch experiments that explored –*ex situ*- the thermodynamics and

kinetics of binding indirectly by quantifying the difference in the concentration of organoarsenicals before and after adsorption/desorption.

Shimizu *et al* investigated the adsorption kinetics of arsenate, MMA and DMA on soils and found it to be biphasic with fast and slow sorption steps due to electrostatic attraction, and diffusion or adsorption on sites with different reactivity, respectively (58). Sorption rates increased in this order: DMA < MMA < arsenate, which was explained based on the molecular structural differences among these molecules (58). DMA has two methyl groups and hence lower electrostatic attraction to positively charged surface as compared to arsenate that has no methyl groups and more deprotonated As-O groups (58).

Solutions of Cl^-(aq) and HPO_4^{2-}(aq) are commonly used in batch desorption experiments to quantify desorption efficiency of methylated arsenicals using these agents and their usefulness in regenerating active sites for recycling adsorbent materials. Studies have shown that phosphate is a more efficient desorbing agent than Cl^-(aq), and increasing the degree of methylation on arsenate increases the percentage of desorbed arsenic (58-60). Previous batch studies also showed that at neutral pH, desorption of methylated and inorganic arsenic by phosphate is not quantitative, and that more is retained by goethite than 2-line ferrihydrite (59). Earlier work on the incomplete desorption of inorganic arsenic from goethite using phosphate was explained by the presence of surface complexes that are resistant to desorption with increase in residence time (61, 62). As discussed by Pigna *et al*, the formation of these complexes can be attributed to different aging mechanisms such as rearrangement of surface complexes, conversion to surface precipitates, sorption reactions on higher energy binding sites,

intraparticle diffusion and penetration into micropores (61). While these conclusions were made from desorption experiments over long times frames (hours-months), they provide insight into the complex desorption mechanism of DMA.

Batch experiments have found that maximum adsorption of inorganic arsenic on goethite occurs around pH 5 which is due to the isoelectric point (the pH at which a particular molecule or surface carries no net electrical charge) of goethite being $8.1 - 8.2$ meaning that at lower pH, the goethite particles are predominantly positively charged and arsenic acid, predominantly present in its anion form will allow for easier adsorption (64). In general, arsenate removal was slightly better in acidic conditions compared to basic conditions (65). The effects of carbonate species in the adsorption of arsenic on iron oxides have also been studied and the presence of carbonate was found to not affect the final amount of arsenic adsorbed, but to reduce the adsorption rate during the early stage of adsorption at pH 8, and enhance the rate at pH 4, and 6 (66).

1.3.2 Mathematical Models used in Describing DMA Adsorption/Desorption

For every adsorption/desorption experiment, mathematical models will be applied to data in order to extract thermodynamic and kinetic parameters. Some of the most common kinetic analysis models are the Langmuir adsorption model used in the kinetic analysis of this thesis (60), the Pseudo-First order rate equation used previously to describe arsenate induced phosphate desorption,

$$r = k_r [As] \tag{1}$$

where [As] is the concentration of the arsenate species in solution, k_r is the rate coefficient or rate constant which is the slope of the r_0 vs. arsenate concentration curve

(67). This equation is based on a 1:1 exchange stoichiometry between the desorbing species and the adsorbed species (67). The Pseudo-Second order equation used to describe arsenic adsorption and desorption

$$r = k_r[As]^2 \qquad (2)$$

The Arrhenius equation

$$k_r = Ae^{-\frac{E_{app}}{RT}} \qquad (3)$$

where A is the Arrhenius pre-exponential term, R is the gas constant, T is the temperature, and E_{app} is the apparent activation energy (68). and the Elovich equation

$$\frac{dq}{dt} = \alpha^{(\ \beta q)} \qquad (4)$$

where q is the amount of adsorbate adsorbed in the time t, and α and β are empirical constants (65).

Thermodynamic studies have been carried out to provide thermodynamic binding constants, $K_{binding}$, by applying the triple layer surface complexation model to adsorption isotherm and pH-envelope data of DMA and p-AsA on hematite and goethite (47). Based on ATR-FTIR data, ligand exchange reactions were constructed to better interpret surface complexes formation. The best fit to the DMA adsorption data was obtained using outer-sphere complex formation, whereas for p-AsA best fit was obtained using two monodentate inner-sphere surface complexes (47).

Another mathematical model used in arsenic adsorption and desorption is the charge distribution multisite surface complexation model (CD-MUSIC), in which surface complexes are not treated as point charges, but are considered as having a spatial charge distribution over their ligands, which are present in two different electrostatic planes (69).

This model has been successfully applied to describe the charge and electrokinetic behavior of TiO_2. At the 0-plane or surface, protons and surface-oriented ligands of adsorbed organic arsenic are placed (70). The 1-plane is the location for the solution-oriented ligands of adsorbed organic arsenic. The charge of adsorbed organic arsenic is distributed between the 0- and 1-plane (70). The 2-plane corresponds to the head end of the diffuse double layer where electrolytes are placed (70). The different planes result in different reactions which can be implemented using their pKa values and creating a tableau which is then inserted into a computer program like MATLAB to theoretically predict surface complexation.

1.3.3 X-ray Adsorption Studies of DMA on Soils and Metal Oxides

Currently, spectroscopic data has been used to obtain evidence for precise evaluation of the sorption reactions at solid/liquid interfaces. X-ray adsorption spectrometry or XAS has been utilized to study the speciation and local structure of arsenic on mineral surfaces with results shown in Table 2. One study gave EXAFS (extended X-ray absorption fine structure) results showing MMA formed bidentate surface complexes on TiO_2 with an As–Ti distance of 3.32 ± 0.01 Å, while DMA formed monodentate complexes with an As–Ti distance of 3.37 ± 0.04 Å (70). The surface charge of TiO_2 as a function of ionic strength exhibited a point of zero charge (PZC) at a pH of 5.8, which was identical to the isoelectric point (IEP), determined using the zeta potential curves (70). The adsorption of MMA and DMA shifted the IEP to a lower pH range, indicating the anionic nature of the adsorption process. Low pH, less than 6, was found favorable for the adsorption of MMA and DMA on TiO_2 and Fe(oxyhydr)oxides (70).

Table 2. Local coordination environment of As determined by EXAFS.

Species	Shell	CN	R (Å)	σ^2	Ref
MMA	As-O	3.0 ± 0.2	1.69 ± 0.01	0.0024 ± 0.0006	70,
	As-C	1.0 ± 0.2	1.90 ± 0.04	0.0002 ± 0.0023	71, 58
DMA	As-O	1.9 ± 0.1	1.69 ± 0.01	0.0034 ± 0.0009	70,
	As-C	1.9 ± 0.2	1.89 ± 0.01	0.0023 ± 0.0014	71, 58
MMA + TiO$_2$	As-O	3.0 ± 0.1	1.69 ± 0.01	0.0018 ± 0.0004	70
	As-C	0.8 ± 0.3	1.88 ± 0.03	0.0053 ± 0.0042	
	As-Ti	1.9 ± 0.4	3.32 ± 0.01	0.0067 ± 0.0015	
DMA + TiO$_2$	As-O	1.9 ± 0.1	1.71 ± 0.01	0.0014 ± 0.0006	70
	As-C	1.9 ± 0.3	1.92 ± 0.02	0.0023 ± 0.0015	
	As-Ti	1.0 ± 0.1	3.37 ± 0.04	0.0064 ± 0.0038	
MMA-FeOOH	As-O	3 (fixed)	1.70 ± 0.008	0.0010 ± 0.0007	58
	As-C	1 (fixed)	1.89 ± 0.01	0.0010 ± 0.0010	
	As-O-O	6 (fixed)	3.12 ± 0.05	0.0069 ± 0.0040	
	As-Fe	1.8 ± 1.1	3.31 ± 0.03	0.0080 ± 0.0020	
DMA-FeOOH	As-O	2 (fixed)	1.71 ± 0.0056	0.0011 ± 0.0005	58
	As-C	2 (fixed)	1.91 ± 0.009	0.0009 ± 0.0004	
	As-O-O	2 (fixed)	3.15 ± 0.02	0.0070 ± 0.0030	
	As-Fe	1.9 ± 0.5	3.30 ± 0.08	0.0069 ± 0.0008	
MMA-Al2O3	As-O	3 (fixed)	1.69 ± 0.007	0.0012 ± 0.0006	71
	As-C	1 (fixed)	1.89 ± 0.008	0.0009 ± 0.0025	
	As-Al	2.1 ± 0.94	3.16 ± 0.022	0.0058 ± 0.0017	
DMA-Al2O3	As-O	2 (fixed)	1.70 ± 0.010	0.0011 ± 0.0004	71
	As-C	2 (fixed)	1.90 ± 0.010	0.0013 ± 0.0007	
	As-Al	2.4 ± 0.60	3.17 ± 0.010	0.0056 ± 0.0015	

The overall results of the studies tabulated above indicated that adsorption did not change the first shell distances and coordination numbers of arsenic with oxygen and carbon, compared to the soluble MMA and DMA forms. As(V) forms bidentate complexes on Fe and Al oxides by ligand exchange with surface water and hydroxyl groups at the mineral surface. However, the As–Ti distance (3.37 ± 0.04 Å) for the DMA surface complex was shorter than the algebraic sum of As–O (1.69 Å) and Ti–O (1.90 Å) (70). This was explained by the formation of hydrogen bonds between the oxygen atom in DMA and the adjacent (protonated) hydroxyl group on TiO_2 surface, which would attract the As tetrahedra closer to the surface. The bond distance of As–Ti in the MMA adsorption sample (3.32 ± 0.01 Å) was comparable to As–Fe (3.31 ± 0.03 Å) and As–Al (3.16 ± 0.022 Å) distances; its coordination can be described as corner sharing between As tetrahedral and edge-sharing pairs of TiO_2 octahedra (70).

EXAFS studies also reported As-Fe interatomic distances in bidentate DMA(ads) and iAs(ads) to be 3.3 and in the range 3.23-3.37 Å, respectively (58, 71). It is important to highlight that samples prepared for EXAFS allow for at least 24 hr equilibrium time with the aqueous phase before a paste-like sample with unknown amount of water is prepared for measurements. Also, the coordination number (CN) used in fitting the raw EXAFS data is one of the fitting parameters along with interatomic distances. In most cases, least-squares fitting using a CN of 2 produces the best least squares fit to the data, which is not surprising given that fitting procedures in EXAFS data analysis is based on the crystallographic data reported for arsenate salts. It is rarely reported that a CN of 1 for monodentate arsenic-containing complexes would fit raw EXAFS data.

1.3.4 Infrared Studies of DMA on Soils and Metal Oxides

Through IR studies the spectral features of arsenate adsorption on goethite specifically have been identified. Bands at 797 and 893 are characteristic of goethite alone and have been said to arise due to the γ and δ –OH bending modes of out and in plane modes (72). An intense band at 3179 is due to the bulk –OH stretching. The symmetric stretching of Fe-O is present as a band at 613. When arsenate is adsorbed bands at 862 and 830 are present and can be assigned to $HAsO_4^-$ ion and As-O-Fe groups (72). These have been concluded as being indicative of arsenate not only binding through Fe-O bonding, but also by non-surface complexes As-O bonds of adsorbed arsenate species (72).

ATR-FTIR data has suggested the simultaneous formation of inner- and outer-sphere DMA complexes which gives rise to spectral components in the range of 700-880cm^{-1} (45, 60). Low frequency components at 771 and 768cm^{-1} have major contributions from inner-sphere complexes, and hence are assigned to υ(As-OFe) (60). Spectral components observed at 791cm^{-1} have been assigned to υ(As-O---H) from uncomplexed As-O bonds involved in strong hydrogen bonding as observed from DMA in the solid phases (60). Components around 840cm^{-1} have been assigned to υ(As=O) from free As=O groups (60). Components at 876cm^{-1} was assigned to υ(As=O) in outer sphere complexes as a result of the involvement of the second As-O group in DMA in strong hydrogen bonding that decreases electronic delocalization (60). When desorption is carried out, the feature at 800cm^{-1} is due to a decrease in the concentration of $\equiv$FeOH or $\equiv FeOH_2^+$ sites on FeOOH films as a result of DMA adsorption through hydrogen bonding or ligand exchange mechanisms (60).

Overall, studies have not utilized ATR-FTIR very often except as complementary studies, towards the better understanding of the adsorption and desorption mechanisms of arsenic species. The initial adsorption and desorption time frame has also not been studied in detail and considering that it is the relatively short time frame where most of the adsorption/desorption chemistry takes place, it is important to conduct studies to better understand what is occurring in that time frame. The literature also highlights the need for kinetic studies on the adsorption and desorption behavior of methylated organoarsenicals using *in situ* and surface sensitive measurements.

2. Overview of thesis objectives

In light of the above, the contribution of this thesis is to study the kinetics of adsorption and desorption by Cl⁻ and phosphate species of DMA on goethite and hematite with specific focus on the first 5 minutes of adsorption and desorption. Hematite and goethite films were deposited on a ZnSe crystal, followed by flowing of different background and adsorbing/desorbing agents solutions for different windows of time. DMA adsorption and desorption were investigated, along with phosphate adsorption in the presence and absence of DMA and arsenate. DMA results were then compared to arsenate results to obtain insight into the different binding mechanisms of organic and inorganic arsenic compounds as well as surface complexes formed.

2.1 Principles of ATR-FTIR as a surface sensitive technique

The surface-sensitive attenuated total reflection Fourier transform infrared technique (ATR-FTIR) was employed for *in situ* spectroscopic identification of the surface complexes formed. The technique measures the changes that occur in a totally internally reflected infrared beam when the beam comes in contact with a sample (see Figure 5). This IR beam is directed onto the crystal at a given angle of incidence and its internal reflectance creates an evanescent wave that extends beyond the surface of the crystal and into the sample in contact with it. Therefore, in regions of the IR spectra where the sample absorbs energy, the wave will be altered, and upon reaching the detector produces a spectrum that depicts that change. For ATR-FTIR to successfully produce results, the following requirements must be met: the sample must be in direct contact with the ATR crystal, because the evanescent wave only extends beyond the

29

crystal 0.5 μ - 5 μ; and the refractive index of the crystal must be significantly greater than that of the sample or else internal reflectance will not occur and the light will be transmitted rather than internally reflected in the crystal.
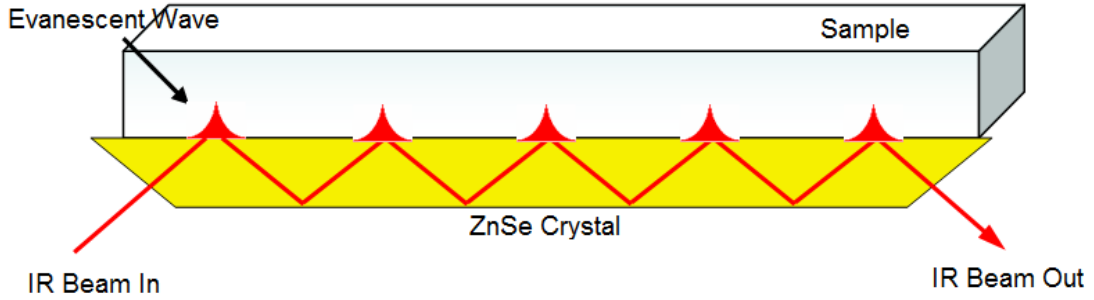
Figure 5. ATR-FTIR schematic.

$$d_p = \frac{\lambda_{IR}}{2\pi(n_1^2\sin^2\theta - n_2^2)^{1/2}} \tag{5}$$

$$b = Nd_p \tag{6}$$

$$N = \frac{\text{Length of Crystal}}{2\tan\theta(\text{Thickness of Crystal})} \tag{7}$$

Where λ_{IR} is the wavelength of IR light; n_1 is the index of refraction of the crystal which is 2.4 for the ZnSe crystal used; n_2 is the index of refraction of the sample which is 1 due to the solutions all being made using Millipore water. θ is the angle of incidence which was calculated to be 60°; N is the number of reflections which was calculated to be 4; b is the total path length which was calculated to be 3.51 μm; and d_p is the depth of penetration which was calculated to be 0.88 μm The short path length is needed to be able to subtract the water signal in our spectra to look at the signal of the solutes in water.

3. Experimental

3.1 Reagents

Solutions of adsorbing and desorbing agents were prepared fresh for every experiment to avoid carbonate build-up over time and used promptly thereafter. DMA and arsenate solutions (sodium cacodylate trihydrate, $C_2H_6AsO_2Na \cdot 3H_2O$, Sigma-Aldrich, and sodium arsenate, $AsO_4HNa_2 \cdot 7H_2O$, ACS reagent, J.T. Baker, used as received) were prepared by first dissolving the powder in 0.01M KCl solutions made using 18 MΩ Millipore water with continuous mechanical stirring, and then adjusted to pH 7 using dilute and concentrated NaOH and HCl solutions (6 N, Ricca Chemical). *Caution: DMA is highly toxic via inhalation and skin contact and is a carcinogen.* Solutions of 0.01M KCl and phosphate (99.99%, Na_2HPO_4, Sigma-Aldrich) adjusted to pH=7 were used for the desorption experiments. At this pH, the most dominant species of DMA is the deprotonated form and the most dominant phosphate species are $H_2PO_4^{1-}$(aq) and HPO_4^{2-}(aq) due to phosphoric acid having pKa values at 2.15, 7.20, and 12.35. Phosphate species will be indicated by HPO_4^{2-} throughout this discussion section. Once the solutions were prepared, the experiment was started and the solutions not used immediately were covered with parafilm and kept on the lab bench until needed.

The Fe-(oxyhydr)oxides used herein are hematite and goethite (α-Fe_2O_3, >99.9%, Nanostructured and Amorphous Materials). Characterization of BET surface area, particles' shape and size, and isoelectric points was reported earlier as 19 m^2/g, 67 nm average diameter, and 8.6 for spherical α-Fe_2O_3 particles, and 21 m^2/g, 0.1 – 0.9 μm and 88 for needle-shaped α-FeOOH particles respectively (56). Details on the experimental

procedure for preparing thin Fe-(oxyhydr)oxide films on the ATR internal reflection element (IRE) are explained below.

3.2 Film preparations on ATR-FTIR crystal

The film deposition method used has been modified from the literature. The criterion used to test this method is the stability of the deposited film when in contact with water throughout the experimental time, which ranged from 4 to 8 hours. This deposition procedure yielded reproducible films in good and uniform contact with the ATR crystal and was verified by measuring the baseline-corrected heights of the bands between $700 - 1000$ cm^{-1} assigned to in-plane and out-of-plane deformation modes of surface OH groups. α-Fe$_2$O$_3$ films were prepared by making a slurry of 14.8, 8, and 6 mg sample in an 1.5 mL water/ethanol mixture (1 : 0.4 (v/v)), which was ultrasonicated for 1 hr. All of the solution was then spread over a clean and dry ZnSe ATR crystal and allowed to dry overnight in air at room temperature. Goethite (α-FeOOH) slurry was prepared using a 16 mg sample of ground goethite (Wig-L-Bug, 6 min), in 0.75 mL of ethanol. The slurry was ultrasonicated for 1 hour and then deposited on a clean and dry ZnSe ATR crystal and allowed to dry overnight in air at room temperature. ATR-FTIR spectra of the dry films were acquired at the beginning of every experiment. Water adjusted to the desired pH and ionic strength was then flowed in excess amounts into the flow cell containing the dry deposited films to remove the loosely bound particles. Most of these particles were from the top layers of the film, and not those probed by the evanescent wave.

3.3 Experimental Procedure:

ATR-FTIR spectra were collected as a function of time on freshly prepared hematite and goethite films using a HATRPlus accessory (Pike Technologies) installed in a Nicolet 8700 FTIR spectrometer (Thermo Instruments) equipped with an MCT detector. The Fe-(oxyhydr)oxide films were directly deposited on a 60° ZnSe crystal IRE (80×10×4 mm) housed in a 100 μL ATR flow cell and allowed approximately 12hrs to dry. Throughout the experiment, single beam ATR-FTIR spectra were collected at 8 cm^{-1} resolution by averaging 15 scans as a function of time for the first 25 min and 100 scans for up to 80 min for adsorption only. The solutions were flowed at a rate of 1 mL/min and 2 mL/min across the Fe-(oxyhydr)oxide films using Tygon tubes (0.8 mm I.D., Maserflex) and a compact pump (Masterflex L/S). Initially, 0.01M KCl were flowed to allow the film to reach equilibrium, and ensure no film loss throughout the experiment. DMA adsorption was then carried out for up to 80min followed by desorption for 25 or 10min depending on the desorbing agent concentration. Each adsorption and desorption spectra was referenced to the last KCl single beam to give absorbance files with the DMA signal easily examinable. The absorbance files were analyzed at time differences as low as 10sec and as high as 15min. The heights of the different most prominent peaks were then analyzed and plotted as a function of time. The smaller time frame analysis were carried out specifically for the fast step of the adsorption/desorption reactions which is from time 0 to 5min. Desorption behaviour experiments by electrolyte and phosphate solutions were conducted at pH7 and I=0.01 M. To determine the uncertainty in the measurements, experiments were repeated 3-5 times on freshly-prepared films.

4 Results:

4.1 Attenuated Total Reflection Fourier Transform Infrared of Aqueous Dimethylarsinic Acid:

4.1.1 Spectra

The aqueous phase spectra of DMA(aq) were collected as a function of concentration. Solutions were flowed over the crystal using a flow system pump for approximately 12 minutes at a rate of 1 mL/min. A scan of the KCl background solution was taken once an equilibrium flow was reached and each DMA scan was referenced to this scan such that the only spectral features remaining would be due to DMA in solution alone. Figure 6 shows the spectral features obtained, with peaks at 877 cm^{-1} assigned to the rocking motion of the methyl groups present in DMA ($\rho(CH_3)$) and 830 cm^{-1} which is assigned to the stretching vibration of the As–O bond $\upsilon(As-O)$ (87).
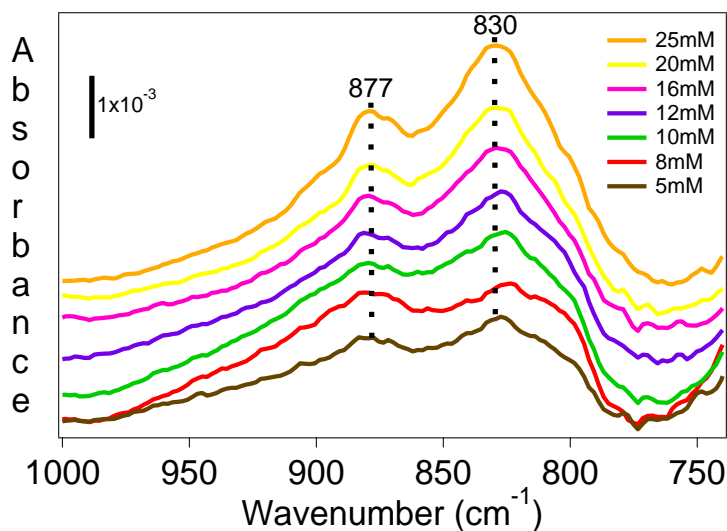
Figure 6. Representative ATR-FTIR spectra of DMA in solution at different concentrations at pH 7, $I = 0.01$ M.

4.1.2 Calibration Curve

From each spectrum, the peak height at 830 cm^{-1} was obtained and plotted against the corresponding DMA concentration. This calibration curve, seen in Figure 7, can also be used to determine the molar absorptivity of DMA(aq) due to the linear relationship it deduces:

$$\text{Absorbance} = b(\text{DMA Concentration}) \qquad (8)$$

Where b is the slope of the line and is equal to 1.8e-4 mM^{-1}. Based on Beer's law which relates absorbance to concentration in a linear fashion, the y-intercept is forced through 0. A 0 y-intercept was also set in order to give low weight to the low concentration absorbances which showed higher variation than the high concentrations in the obtained absorbances in order to extract a correct slope value.
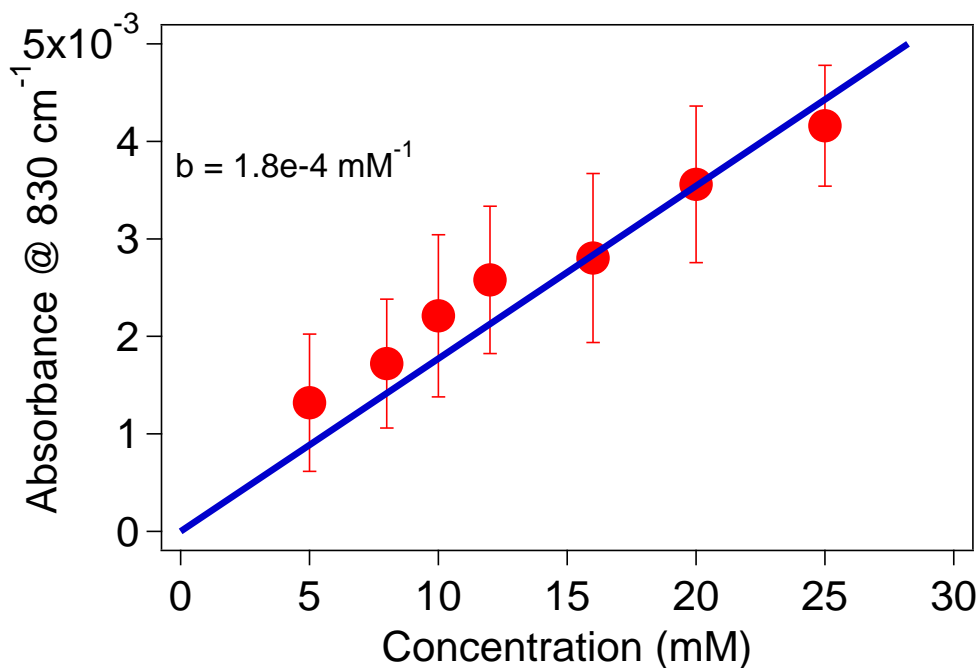
Figure 7. DMA calibration curve using 1 mL/min flow rate, pH 7 and *I* = 0.01 M. DMA concentrations used were 5 mM, 8 mM, 10 mM, 12 mM, 16 mM, 20 mM, and 25 mM; 3 trials averaged.

A concentration for adsorption experiments could be chosen based on the calibration curve such that spectral features obtained throughout the experiment would be due to adsorbed DMA only, and no influence from DMA(aq) would take place. Therefore, the concentrations for DMA adsorption experiments used were 1mM and 0.5mM, which, from Figure 7, are well below the detection limit of the flow cell used which contained the ZnSe crystal for all measurements.

4.2 Adsorption Kinetics of Dimethylarsinic Acid on Hematite and Goethite:

4.2.1 Spectra

DMA adsorption experiments were carried out on hematite and goethite as a function of time. From the spectra, shown representatively in Figure 8, simultaneous formation of inner- and outer-sphere DMA(ads) species gave rise to spectral components in the range 700-800 cm^{-1}. The low frequency component at 767 cm^{-1} in Figure 8b had major contributions from inner-sphere complexes and was assigned to v(As-OFe). Components at 791 and 793 cm^{-1} were assigned to v(As–O---H) from uncomplexed As-O bonds involved in strong H-bonding as observed for DMA in the solid phases. Additionally, components around 840 and 833 cm^{-1} were assigned to v(As=O) from free As=O groups, with bond order of around 1.5. Moreover, components at 877 and 870 cm^{-1} were assigned to v(As=O) in outer-sphere complexes as a result of the involvement of the second As-O group in DMA in strong H-bonding that decreased electronic delocalization. As a result, none of these spectral components can be exclusively assigned to inner or

outer-sphere complexes alone; hence the kinetic data was analyzed as a function of spectral components.
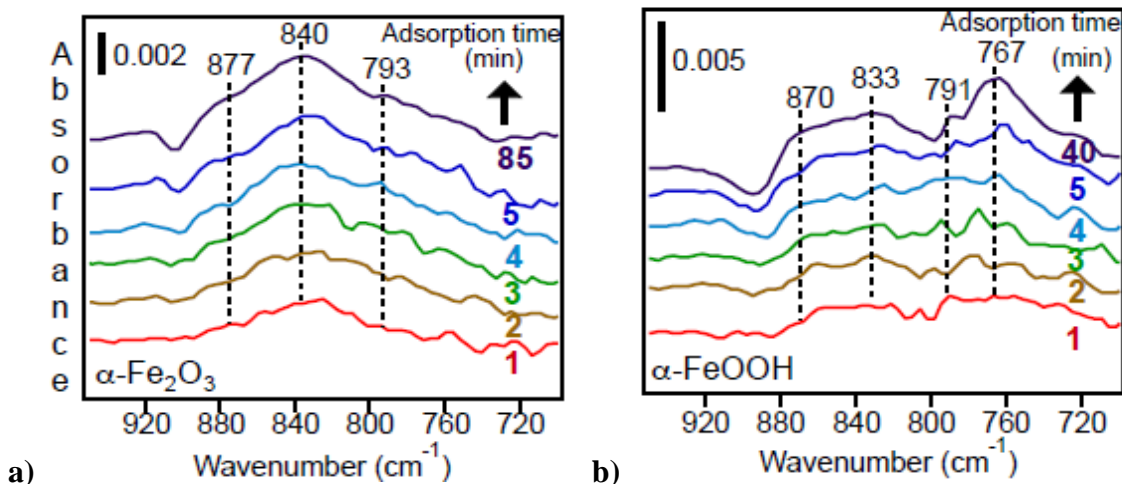
Figure 8. a) ATR-FTIR DMA adsorption spectra on a 6 mg hematite film b) ATR-FTIR DMA adsorption spectra on a 16mg goethite film; all adsorption experiments were done using 1 mL/min flow rate, pH 7, $I = 0.01$ M, and 0.5 mM [DMA].

Using the absorbance of components 840 and 833 cm^{-1}, surface coverage of DMA(ads) can be quantified. According to published DMA adsorption isotherms, at pH 7 and I=0.01 M KCl, the surface coverage of DMA(ads) at 0.5 mM was equivalent to 1 and 0.7×10^{13} molecule/cm^2 on α-Fe$_2$O$_3$ (14.8 mg film), and α-FeOOH (16 mg film), respectively (47). This is equivalent to roughly 0.5 monolayer relative surface coverage when compared to the maximum of 3(1) and 2(0.5)$\times 10^{13}$ molecule/cm^2 reported earlier (46). By extrapolation, using 0.5 mM DMA (aq) and a 6 mg α-Fe$_2$O$_3$ film resulted in about 80% surface coverage of DMA(ads).

4.2.2 Kinetic Curves

Baseline-corrected ATR absorbances [A(v)] of the spectral components shown above were used to generate kinetic curves of absorbance at a given wavenumber versus time and these plots are shown below for the most prominent peaks. All peaks resulted in similar kinetic curves.

To extract apparent adsorption rates from these experimental data, the Langmuir adsorption model was used. The model makes three assumptions: there is one type of adsorption site (they are equivalent and uniform), after all the sites are filled, adsorption ends (adsorption is complete after a monolayer is formed), and if one site is undergoing adsorption, the site next to it can undergo either adsorption or desorption, the processes are uncooperative. The Langmuir adsorption kinetic model eq. (10) derived for the reaction shown in eq. (9)

$$DMA(aq) + \text{ empty site1} \underset{k_{des1}}{\overset{k_{ads1}}{\rightleftharpoons}} DMA(ads, 1) \tag{9}$$
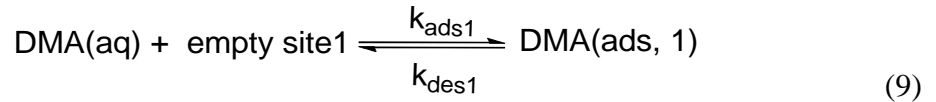
$$\theta_1(t) = b_1(1 - e^{-r_{obs1} \cdot t}) \tag{10}$$

where $\theta_1(t)$ is the relative surface coverage of a given surface complex of DMA(ads), b_1 is a collection of constants that equal $k_{ads1}[DMA(aq)]/r_{obs1}$, and $r_{obs1} = k_{ads1}[DMA(aq)] + k_{des1}$. Because $\theta_1(t)$ is equivalent to $A(v)/A_{max}(v)$, eq.(10) can be rewritten in terms of $A(v)$: $A(v) = b'_1(1 - e^{-r_{obs1}t})$, where $b'_1 = A_{max}(v)b_1$. The latter equation is referred to as the 1-site model and used to fit the experimental data in Figure 9. The linear form of this model is: $\ln(1 - A(v)/b'_1) = -r_{obs1}t$. Values of b'_1 were taken by averaging the data points in the plateau region. When the experimental data was normalized and plotted in the linear form as shown in the lower panel of Figure 9, it became evident that the data are

best fit with two lines instead of one, suggesting two kinetic regions for the adsorption of

DMA(aq). The slopes of these lines are referred to as r_{obs1} (fast) and r_{obs2} (slow).
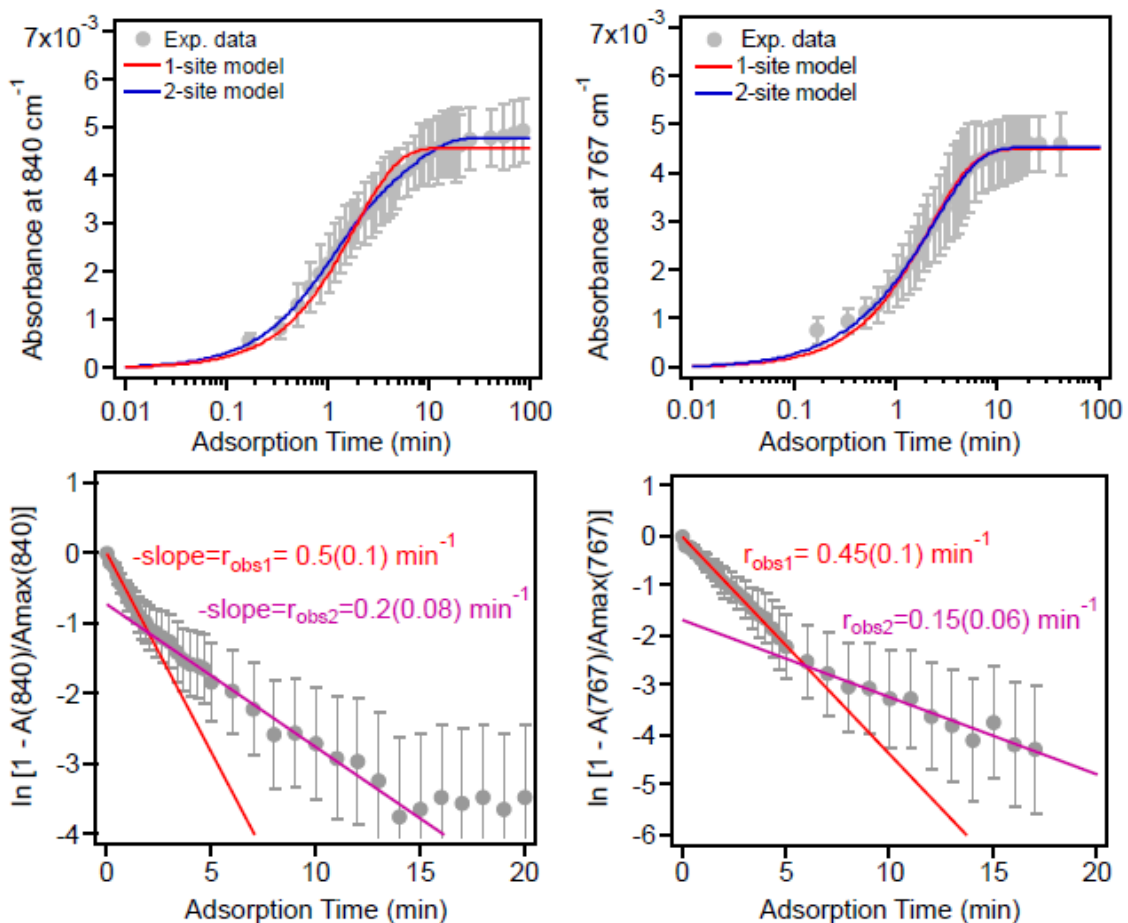
Figure 9. DMA adsorption kinetics on hematite (6 mg, left panel) and goethite (16 mg,

right panel). Baseline-corrected ATR absorbances at 840 and 767 cm^{-1}, respectively, were

used to generate kinetic curves (filled markers). Lines through the data represent

Langmuir adsorption kinetic models. Error bars represent the standard deviation from

averaging 8 and 4 experiments, respectively. Experimental conditions: pH = 7, $[DMA_{(aq)}]$

= 0.5 mM, Flow Rate = 1 mL/min, I = 0.01 M.

While the single exponential 1-site model resulted in a relatively good fit to the experimental data, a two-exponential, 2-site model, $\theta_{total}(t) = b_1(1 - e^{-r_{obs1}t}) + b_2(1 - e^{-r_{obs2}t})$, was used as well in light of the behaviour observed in the normalization and further linearization of the data that showed two distinct kinetic regions.

Figure 10 shows values of r_{obs1} and r_{obs2} from kinetic experiments on the adsorption of DMA(aq) on α-Fe$_2$O$_3$ at pH 7 and I=0.01 M KCl from the analysis of spectral components at 877, 840 and 793 cm^{-1} assigned to DMA(ads) as a function of (a) flow rate of DMA(aq) using 0.5 mM DMA(aq) and 6 mg film, (b) [DMA(aq)] using 1 mL/min flow rate and 6 mg film, and (c) film mass of α-Fe$_2$O$_3$ using 1 mM DMA(aq) and 1 mL/min flow rate. Figure 10(a) shows r_{obs1} have similar values for the three spectral components, and are independent of the flow rate of DMA(aq).

The same observation can be made for the values of r_{obs2} using 1 mL/min flow rate. However, using a higher flow rate (2 mL/min) results in a reduction of r_{obs2} of the 877 cm^{-1} component suggesting that it has a large contribution from weakly bound outer-sphere DMA(ads). This is because using a higher flow rate increases desorption and decreases adsorption kinetics of weakly bound species. The similar values of r_{obs2} for the spectral components 840 and 793 cm^{-1} indicate that both originate from similar DMA(ads) complexes.

The contribution of diffusion of DMA(aq) into the porous hematite films to the values of r_{obs1} and r_{obs2} was also investigated using 1 mM DMA(aq) and 1 mL/min flow rate. Figure 10(b) shows the dependency of r_{obs1} and r_{obs2} on the mass of α-Fe$_2$O$_3$. After experimenting with different masses, 6 mg was the minimum mass that could be deposited uniformly with reproducible thickness that was relatively stable over the course

of an experiment. The data show that r_{obs1} values were relatively higher using 6 mg than 14.8 mg films, and data from 8 mg fall in between. If the diffusion rate of DMA(aq) from the top hematite layer to that accessed by the evanescent wave contributes to the overall r_{obs1}, it will result in a relative decrease in r_{obs1} values.
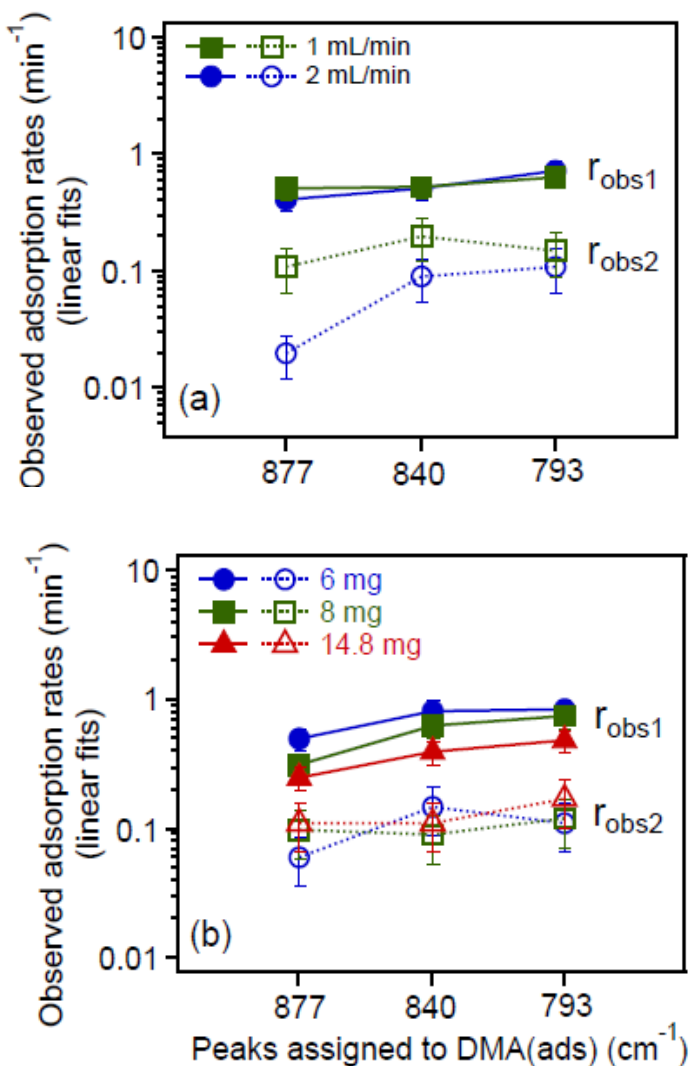
Figure 10. Observed adsorption rates of DMA(aq) on α-Fe$_2$O$_3$ at pH 7 and $I = 0.01$ M KCl from the analysis of spectral components at 877, 840, and 793 cm^{-1} assigned to DMA(ads) as a function of (a) flow rate of DMA(aq) using 0.5mM DMA(aq) and 6 mg film, and (b) film mass of α-Fe$_2$O$_3$ using 1mM DMA (aq) and 1mL/min flow rate.

41

Earlier published work measured the thickness of 14.4 mg hematite films to be

$11(2.4) \times 10^{-4}$ cm, which is thicker than the effective penetration depth of the evanescent

wave at 837 cm^{-1} ($6.1(3) \times 10^{-4}$ cm) (56). Varying the mass of the hematite film deposited

on the ATR crystal varied the thickness such that the bulk density remains constant.

Hence, the thickness of the 6 mg films is estimated to be ca. 5×10^{-4} cm. Based on these

calculations, diffusion has minimum contribution to the values of r_{obs1} from the 6 mg

films. As for the values of r_{obs2}, Figure 10(b) shows that there is no clear dependency of

r_{obs2} on film mass. This is not surprising as values of r_{obs2} are extracted from kinetic data

collected at longer adsorption times (t > 5 min).

Moreover, the dependency of the observed adsorption rates on [DMA$_{(aq)}$] using a

6 mg film of α-Fe$_2$O$_3$ and 1 mL/min flow rate is shown in Figure 11 from the analysis of

the three spectral components 877, 840 and 793 cm^{-1}. According to $r_{obs1} = k_{ads1}$[DMA$_{(aq)}$]

+ k_{des1} , a linear trend is expected between values of r_{obs1} and [DMA$_{(aq)}$]. Linear least

squares fits of the experimental data will yield values for the adsorption rate constant,

k_{ads1}, and desorption rate constant, k_{des1} as shown in Table 3. The latter value is

equivalent to k'$_{des}$, where Cl$^-$(aq) is the desorbing agent. There was no clear dependency

of r_{obs2} on [DMA(aq)] found. Based on the diffusion results as well as the rate constant

analysis, for the rest of the studies that investigated the desorption behavior of

DMA(ads), 0.5 mM DMA(aq) and 6 mg hematite films were used.
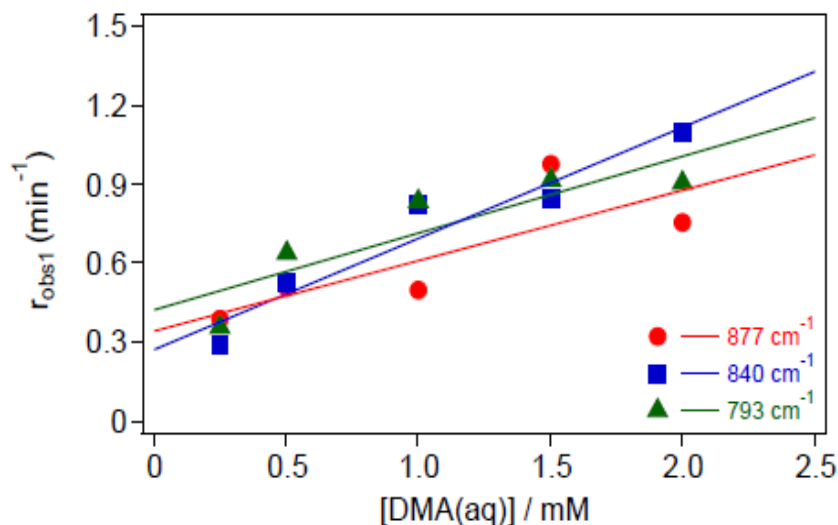
Figure 11. Observed adsorption rates of DMA(aq) on α-Fe$_2$O$_3$ at pH 7 and $I = 0.01$ M KCl using 1 mL/min flow rate and 6 mg film as a function of [DMA$_{(aq)}$]. Error bars were omitted for clarity ($\pm 40\%$).

Table 3. Best fit parameters from linear least squares fits to the experimental data of r_{obs1} versus [DMA$_{(aq)}$] shown in Figure 11. $K_{eq1} = k_{ads1}/k_{des1}$; numbers in parentheses represent $\pm\sigma$.

Peak (v)	Slope (k_{ads1}) $min^{-1}mM^{-1}$	Intercept (k_{des1}) min^{-1}	$K_{eq1}/Lmol^{-1}$	$log(55.5K_{eq1})$
877	0.3(0.1)	0.3(0.15)	1000(601)	3
840	0.4(0.15)	0.3(0.1)	1333(669)	3.1
793	0.3(0.1)	0.4(0.15)	750(376)	2.9

At pH 7, the deprotonated form of DMA is the most dominant species in the aqueous phase. Surface sites at this pH are a mix of neutral ($\equiv$FeOH) and positively charged ($\equiv$FeOH$_2^+$) on the Fe-(oxyhydr)oxides used herein, with a higher concentration of the latter given that their isoelectric point is around 9. Hence, ligand exchange

43

reactions between surface sites and incoming DMA molecules are driven by favorable electrostatic interactions. Analysis of the adsorption kinetics of DMA(aq) on the Fe-(oxyhydr)oxides used herein shows that two adsorption rates are needed to model the experimental data reasonably well. Values of r_{obs2} are a factor of 2 less than r_{obs1}, which might be interpreted as following: the initial phase of adsorption (within the first 5 min) correspond to fast ligand exchange between DMA(aq) and surface sites with fast leaving groups (e.g. H_2O in sites $\equiv FeOH_2^+$) driven by electrostatics. It is very likely that such fast exchange will result in the formation of inner-sphere monodentate DMA(ads) first. It is unlikely that a bidentate DMA(ads) will form at short adsorption times because the likelihood for two adjacent surface sites to have fast leaving groups is low at this pH. Hence, during longer adsorption times (t > 5 min), the monodentate complex might be transformed to a bidentate, or the latter complex forms directly from DMA(aq) at slower rates.

Electrostatic attraction also drives the formation of weakly bound outer-sphere complexes as suggested from the adsorption kinetics measurements using 2 mL/min flow rate of DMA(aq), particularly from the analysis of the 877 cm^{-1} spectral component. Values of r_{obs2} from the time-profile of this spectral component were found to be more sensitive to faster flow rate than r_{obs1}. From the dependency of r_{obs1} on [DMA(aq)] from the hematite data, we were able to extract values of k_{ads1} = 0.4(0.15) $min^{-1}mM^{-1}$, which is equivalent to *ca.* 7(2.5) $Lmol^{-1}s^{-1}$, and k_{des1} = 0.3(0.1) min^{-1} (0.005(2) s^{-1}) from the 840 cm^{-1} data (Table 3) where the number in parentheses represents $\pm\sigma$. When the value of k_{des1} is normalized to the concentration of the background solutions containing Cl^-(aq), a value of 30 $min^{-1}M^{-1}$ was obtained, which is very close to those obtained from the

desorption experiments using Cl⁻(aq) as a desorbing agent (see values of $k^`_{des}$ in Tables 4 and 5 below). Since the binding equilibrium constant, K_{eq}, can be extracted from rate constants through $K_{eq} = k_{ads}/k_{des}$, using the above values a value of 1400(690) Lmol⁻¹ [or $\log(55.5K_{eq}) = 3.2(2.8)$] was obtained, where the number in parentheses represents $\pm\sigma$. Earlier work reported a value of $\log K = 4.3$ for the combined isotherm and envelope data of DMA adsorption on hematite and 5.0 for goethite by applying a triple layer surface complexation model assuming outer-sphere complex formation only (47). Both values of K_{eq} are in close agreement, and lower than those reported for arsenate from pressure-jump kinetic experiments ($\log K = 5.35$ from step 1) and surface complexation models (74).

As discussed above, the results from *in situ* measurements of surface complex formation also reflect the biphasic adsorption kinetics seen in previous studies of DMA with minimum contribution from diffusion over the time frame of our measurements. Hence, the kinetics is best described using two rates of adsorption compared to a single adsorption rate derived from assuming second order kinetics. While there are differences in number and type of coordinated hydroxyl groups between hematite and goethite involved in the ligand exchange with arsenicals, the similarities in the values of DMA adsorption and desorption rates reported herein between the two Fe-(oxyhydr)oxide confirms that DMA accesses similar reactive sites and forms similar types of surface complexes on both solids.

4.3 Desorption Kinetics of Dimethylarsinic Acid from Hematite and Goethite:

4.3.1 Spectra

After each DMA(aq) adsorption experiment, desorption kinetics of DMA(ads) was measured using Cl^-(aq) and HPO_4^{2-}(aq) solutions as desorbing agents (referred to as A(aq) below). Figure 12 shows ATR-FTIR absorption spectra collected as a function of time and desorbing agents for the desorption of submonolayer DMA(ads) from α-Fe_2O_3 and α-FeOOH. Using 0.01 M Cl^-(aq) as a desorbing agent (left), any of the labeled spectral components can be used to generate kinetic curves. However, using HPO_4^{2-}(aq) solutions as desorbing agents (center and right) resulted in the formation of phosphate surface complexes that might contribute to the absorbance of labeled spectral components assigned to DMA(ads). Hence, to decide which spectral component has minimum contribution from phosphate surface complexes, control spectra were collected for the adsorption of 10^{-4} and 10^{-3} M HPO_4^{2-}(aq), respectively, on freshly prepared α-Fe_2O_3 and α-FeOOH films. Based on the comparison between solid and dashed lines in the center and right columns of Figure 12, kinetic curves were generated from components at 840, 793, 775 cm^{-1}, and 840 and 793 cm^{-1} using 10^{-4} and 10^{-3} M HPO_4^{2-}(aq) and α-Fe_2O_3 films, respectively. For α-FeOOH films, kinetic curves were generated from components at 833, 767 cm^{-1}, and 767 cm^{-1} using 10^{-4} and 10^{-3} M HPO_4^{2-}(aq), respectively.
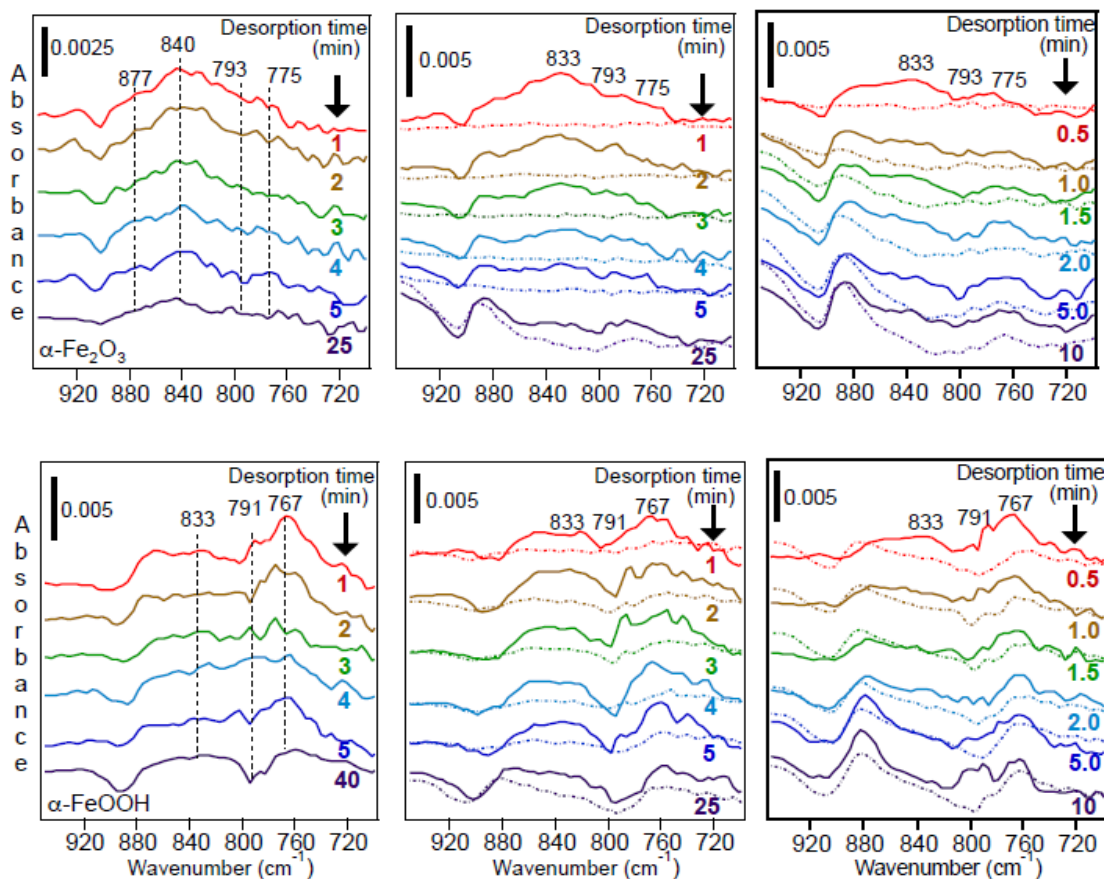
Figure 12. ATR-FTIR absorption spectra collected as a function of time for the desorption of submonolayer DMA(ads) from α-Fe$_2$O$_3$ (6 mg film, upper panel) and α-FeOOH (16 mg, lower panel). Spectra were collected at pH 7 and 1mL/min flow rate of the following desorption agents: 0.01 M Cl$^-$(aq) (left), 10^{-4} M (center), and 10^{-3} M HPO$_4^{2-}$ (aq) (right), respectively. Dashed lines in center and right panels represent control spectra collected for the adsorption of 10^{-4} and 10^{-3} M HPO$_4^{2-}$ (aq), respectively, on freshly prepared films.

Phosphate surface complexes give rise to spectral components in the range 1300 – 900 cm^{-1}, as shown in Figure 16 which increase as a function of desorption time. This

range contains infrared absorbances due to the stretching vibrations (ν) of the uncomplexed P-O and P-OH, and P-O-Fe bonds in adsorbed phosphate. The surface structure of adsorbed phosphate on Fe-(oxyhydr)oxide using ATR-FTIR was reviewed by Elzinga and Sparks (75). Experimental infrared frequencies were correlated with theoretical ones calculated using DFT (77). Based on these earlier studies, it was concluded that under neutral conditions similar to those used herein, deprotonated bidentate and monoprotonated monodentate surface phosphate complexes result in calculated IR frequencies with excellent correlation with experimental data. Hence, spectral components shown in Figure 16 are assigned to $\nu_3(PO_4)$ in the aforementioned inner-sphere complexes due to the splitting in the triply degenerate symmetric stretch ν_3 as a result of reduction in symmetry due to surface complexation.

4.3.2 Kinetic Curves

Figure 13 shows kinetic curves generated from aforementioned spectral components during the desorption of DMA(ads) using 0.01 M Cl$^-$(aq) and 10^{-4} and 10^{-3} M HPO$_4{}^{2-}$(aq). In order to extract desorption rates, we used the simple Langmuir desorption kinetic model, eq.(12), derived for the reaction shown in eq.(11):

$$DMA(ads) + A(aq) \xrightarrow{k_{des}} DMA(aq) + A(ads) \qquad (11)$$

$$\theta(t) = \theta_0 \cdot e^{-k'_{des} \cdot t} \qquad (12)$$

where A(aq) is either Cl$^-$(aq) or HPO$_4{}^{2-}$(aq), $\theta(t)$ is A(ν)/A$_{max}$(ν) A(aq), θ_0 is A$_0$(ν)/A$_{max}$(ν) and k'$_{des}$ = k$_{des}$[A(aq)]. Assuming a constant [A(aq)] is valid since solutions of the desorbing agents are continuously flowing throughout the data collection time.
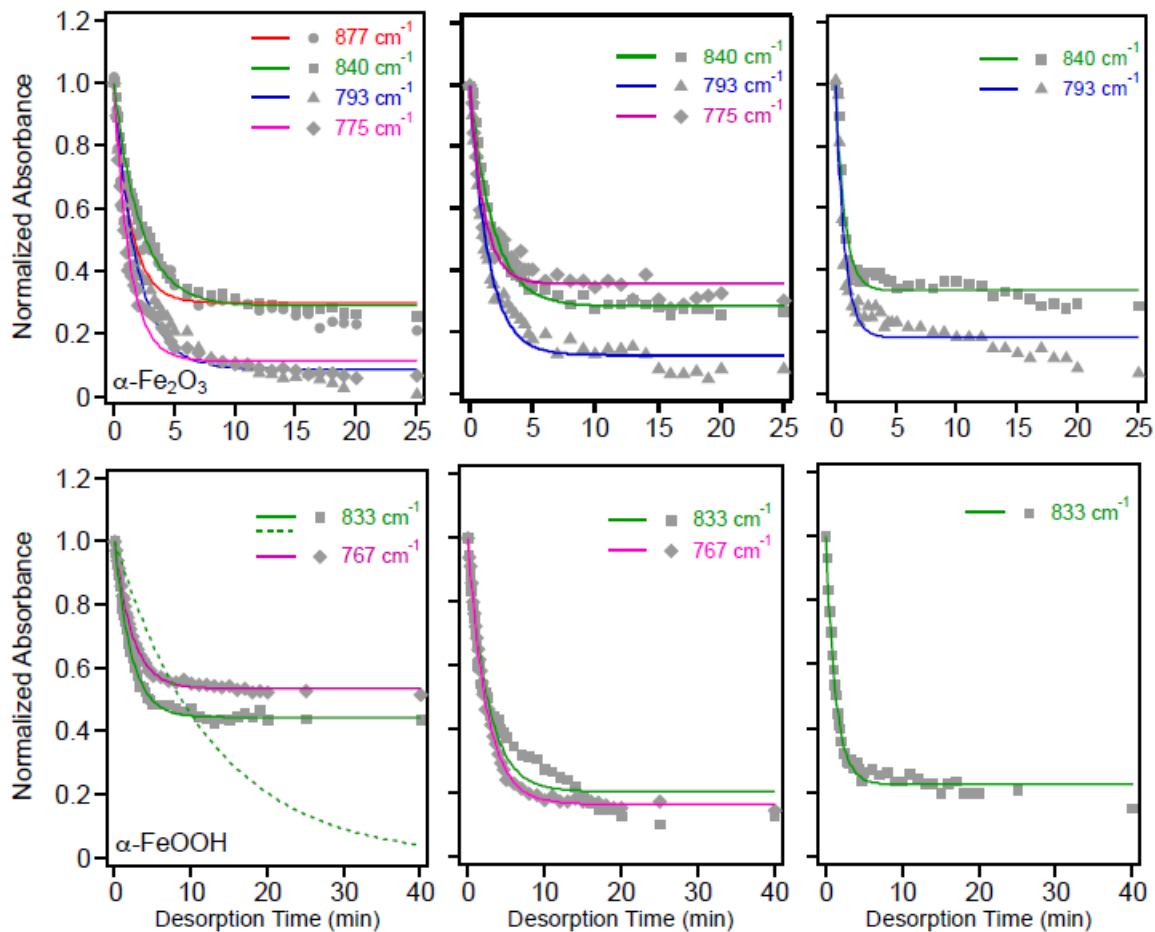
Figure 13. Kinetic curves generated from spectra shown in figure 17 for the desorption of submonolayer DMA(ads) from α-Fe$_2$O$_3$ (6 mg film, upper panel) and α-FeOOH (16 mg, lower panel). The desorption agents are: 0.01 M Cl$^-$(aq) (left), 10^{-4} M (center), and 10^{-3} M HPO$_4^{2-}$ (aq) (right) using 1 mL/min flow rate. Markers represent experimental data (10-20% uncertainty), solid lines represent the modified Langmuir desorption model with re-adsorption [eq.(13)], and dashed lines in the left column represent the simple Langmuir desorption model [eq.(12)]. Error bars omitted for clarity.

Using eq. (12) to fit the experimental data resulted in poor fits (see for example the dashed lines in the left column of Figure 13. This is because the derivation of eq.(12)

does not take into account the possibility for re-adsorption of DMA, which is a likely

process under our experimental conditions where a slow flow rate (1 mL/min) is used,

and unoccupied surface sites with high affinity to DMA(aq) are available since the initial

surface coverage is submonolayer. When the possibility for re-adsorption is included in

the derivation, the modified Langmuir desorption model becomes:

$$\theta = \frac{(k'_{des}\,\theta_0 - k'_{ads})e^{-k_{des}t} + k'_{ads}}{k'_{des}} \tag{13}$$

where $k'_{des} = k_{des}[A(aq)]$ and $k'_{ads} = k_{ads}[DMA(aq)]$. Eq.(13) reduces to eq.(12) if $k_{ads} =$

0. As shown in Figure 13, solid lines represent the modified Langmuir desorption model

with readsorption.

Best fit parameters are shown in Tables 4 and 5, as a function of spectral

components, flow rate and desorbing agent. By visual inspection alone of the data and fits

in Figure 13, the effect of the type and concentration of the desorbing agent is obvious. In

particular, initial desorption rates (t < 5 min) are clearly faster using HPO_4^{2-}(aq) than Cl^-

(aq) solutions. The data suggests that the kinetic behavior of the spectral components

used is similar during the initial phase of desorption, and that these desorbing agents are

capable of releasing inner- and outer-sphere complexes of DMA(ads) at the

concentrations used. When taking the uncertainty of the measurements in Figure 16 into

account, it could be concluded that within the time range of our experiments, DMA

desorption behavior is similar on α-Fe_2O_3 and α-FeOOH.

Table 4. Best fit parameters of the modified desorption/adsorption Langmuir model for the normalized absorbances assigned to DMA(ads) from spectra collected during desorption of DMA(ads) from 6 mg α-Fe$_2$O$_3$ at pH 7.

Desorbing Agent	Peak (ν)	1mL/min		2 mL/min	
		k'_{des} (min^{-1})	k'_{ads} (min^{-1})	k'_{des} (min^{-1})	k'_{ads} (min^{-1})
0.01 M Cl$^-$ (aq)	877	0.7(0.3)	0.2(0.01)	0.8(0.05)	0.3(0.02)
	840	0.5(0.1)	0.1(0.03)	0.4(0.1)	0.1(0.01)
	793	0.5(0.1)	0.05(0.01)	0.8(0.2)	0.1(0.02)
	775	0.8(0.1)	0.09(0.01)	1.0(0.1)	0.2(0.01)
10^{-4} M HPO$_4^{2-}$ (aq)	840	0.5(0.2)	0.2(0.1)	0.7(0.07)	0.04(0.01)
	793	0.7(0.1)	0.09(0.05)	0.6(0.1)	0
	775	0.9(0.2)	0.3(0.1)	1.2(0.01)	0.3(0.2)
3.5x10^{-4} M HPO$_4^{2-}$ (aq)	840	1.2(0.1)	0.2(0.02)	0.6(0.2)	0.05(0.01)
	793	1.0(0.1)	0.04(0.01)	0.6(0.1)	0
	775	1.0(0.1)	0.3(0.05)	0.8(0.01)	0
10^{-3} M HPO$_4^{2-}$ (aq)	840	1.4(0.3)	0.5(0.05)	1.0(0.5)	0.1(0.02)
	793	1.4(0.3)	0.3(0.1)	1.3(0.2)	0.2(0.05)
0.02 M HPO$_4^{2-}$ (aq)	840	2.6(0.3)	0.7(0.1)	2.3(0.01)	0.1(0.05)
	793	3.2(0.4)	0.4(0.05)	2.4(0.2)	0

Table 5. Best fit parameters of the modified desorption/adsorption Langmuir model for the normalized absorbances assigned to DMA(ads) from spectra collected during desorption DMA(ads) from 16 mg FeOOH at pH 7.

Desorbing Agent	Peak (v)	1mL/min		2mL/min	
		k'_{des} (min^{-1})	k'_{ads} (min^{-1})	k'_{des} (min^{-1})	k'_{ads} (min^{-1})
0.01 M Cl$^-$ (aq)	833	0.5(0.1)	0.2(0.01)	0.8(0.1)	0.15(0.01)
	767	0.4(0.1)	0.2(0.1)	0.9(0.1)	0.4(0.1)
10^{-4} M HPO$_4^{2-}$ (aq)	833	0.4(0.1)	0.08(0.02)	0.5(0.05)	0.05(0.02)
	767	0.4(0.01)	0.09(0.05)	0.4(0.02)	0.1(0.01)
3.5x10^{-4} M HPO$_4^{2-}$ (aq)	833	0.6(0.1)	0.08(0.02)	0.5(0.1)	0
	767	0.7(0.1)	0.2(0.1)	0.5(0.1)	0.1(0.02)
10^{-3} M HPO$_4^{2-}$ (aq)	833	0.8(0.1)	0.2(0.05)	0.8(0.1)	0.02
0.02 M HPO$_4^{2-}$ (aq)	833	2.0(0.2)	0.2(0.02)	2.4(0.2)	0

One of the assumptions in the Langmuir desorption model is that the apparent desorption rate constant is dependent on the [A(aq)] with an overall order of 1 and $k_{des} = k_{des}$ [A(aq)]. Therefore, normalizing values of k_{des} to the [A(aq)] should yield a constant value equivalent to k_{des}. Figure 14 summarizes results obtained from this exercise for both α-Fe$_2$O$_3$ and α-FeOOH films as a function of flow rate and spectral components. This figure shows that first, apparent desorption rates are higher using HPO$_4^{2-}$(aq) than Cl$^-$ solutions at pH 7 by 1-2 orders of magnitude, second, dependency of apparent desorption rates on spectral components and flow rates is minimum and within the uncertainty of the measurements, and third, normalizing the apparent desorption rates to the concentrations of HPO$_4^{2-}$(aq) does not yield a constant suggesting a non-unity overall order of desorption with respect to the [HPO$_4^{2-}$(aq)], $k'_{des} = k_{des}$[HPO$_4^{2-}$(aq)]^n, n $\neq$1. To

extract the value of n from the experimental data, we plotted the linear form of the latter

equation, $\ln(k'_{des}) = \ln(k_{des}) + n(\ln [HPO_4^{2-}(aq)]$ as shown in Figure 15 for both Fe-

(oxyhydr)oxide films. Table 6 lists the best fit parameters from linear least squares fits to

the experimental data indicating that n = 0.3(0.04) and $\ln(k_{des}) = 2(0.5)$, independent of

the spectral component used to extract the desorption kinetic parameters.
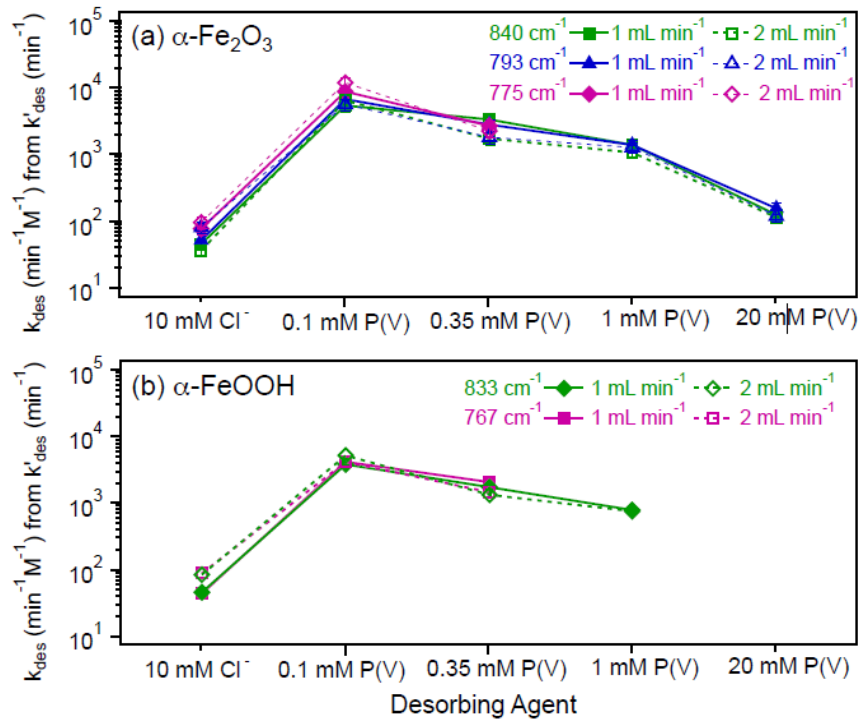
Figure 14. Apparent desorption rate constants, k_{des}, normalized to the concentration of

each desorbing agent, assuming a first order desorption process. Markers represent

experimental data (20% uncertainty). Error bars were omitted for clarity. P(V)

corresponds to $HPO_4^{2-}(aq)$.
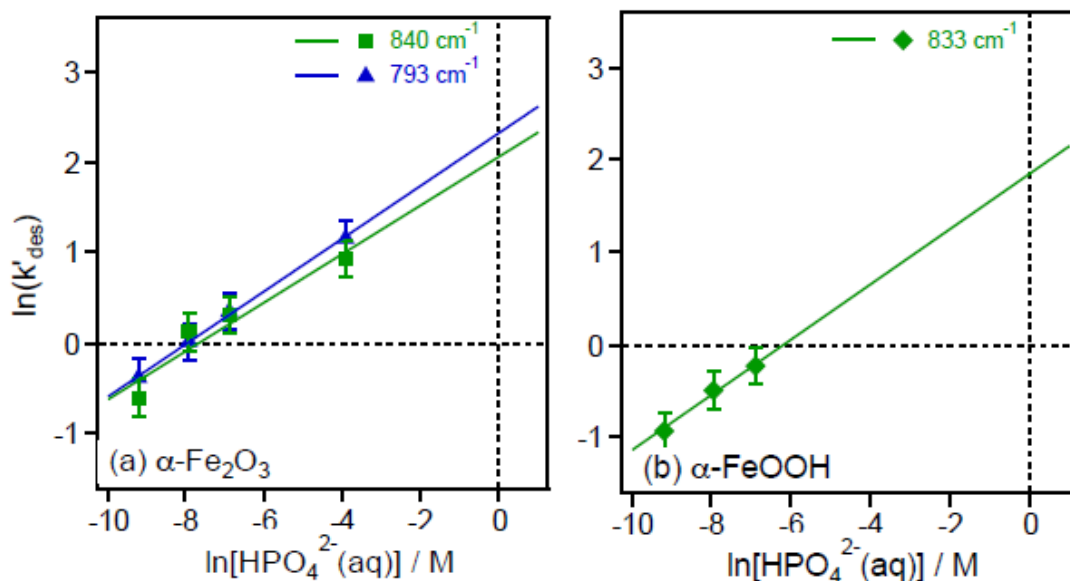
Figure 15. Dependency of apparent desorption rate constants, k'_{des}, obtained from the modified desorption/adsorption Langmuir model, on the concentration of $[HPO_4^{2-}(aq)]$ at pH 7 and 1 mL/min flow rate. Lines through the data represent linear least squares fits.

Table 6 Best fit parameters from linear least squares fits to the experimental data of $\ln(k'_{des})$ versus $\ln([HPO_4^{2-}(aq)])$ shown in Figure 15.

Film	Peak (v)	Flow rate (mL/min)			
		1		2	
		Slope (n)	y-int(lnk$_{des}$)	Slope (n)	y-int(lnk$_{des}$)
α-Fe$_2$O$_3$	840	0.3(0.04)	2.1(0.2)	0.3(0.04)	1.8(0.2)
	793	0.3(0.04)	2.1(0.2)	0.3(0.04)	2.0(0.2)
α-FeOOH	833	0.3(0.04)	2.1(0.2)	0.2(0.1)	1(0.5)

Spectral components below 840 cm^{-1} were used to extract apparent desorption rate constants. These components have major contribution from inner-sphere DMA(ads) and that explains the minimum dependency on the flow rates of the desorbing agents used

herein. Flow rates higher than 2 mL/min were found to physically remove the films in

contact with the ATR crystal, and hence higher flow rates were not used. The spectral

component at 877 cm^{-1} has a major contribution from outer-sphere complexes. Using Cl^{-}

(aq) for the desorption of DMA(ads) from α-Fe$_2$O$_3$, the value of k$`_{des}$(877 cm^{-1}) reported

in Table 4 is slightly higher using 2 rather than 1 mL/min flow rate (0.8(0.05) compared

to 0.7(0.3) min^{-1}, respectively). As mentioned before, this component could not be used

to derive kinetic parameters using phosphate as a desorbing agent because it overlaps

with spectral components arising from phosphate surface complexes. Also, our finding

that apparent desorption rates depend on [HPO$_4$$^{2-}$(aq)] with a non-unity overall reaction

order (n = 0.3) suggests that the desorption mechanism of DMA due to reaction with

HPO$_4$$^{2-}$(aq) is complex, and involves multiple elementary steps necessary to explain the

desorption of inner- and outer-sphere surface complexes of DMA. Potential elementary

steps could be formulated from ligand exchange reactions between phosphate and

monodentate, bidentate and outer-sphere DMA-Fe complexes.

Our group recently reported results from Density Functional Theory (DFT)

calculations on Gibbs free energies of desorption, **ΔG$_{des}$**, of monodentate, bidentate and

outer-sphere DMA-Fe complexes due to reactions with phosphorus species at pH 7 (76).

Values of **ΔG$_{des}$** indicate that desorption favorability of DMA complexes increases in this

order: bidentate < mondentate < outersphere (76)**.** These reactions were constructed to

form bidentate phosphate complexes on the iron oxide clusters. Analysis of the

spectroscopic data of DMA(ads) suggested that the above three types of surface

complexes existed at equilibrium during our studies, and each complex contributes to the

observed spectral components (76). Hence, it is very likely that k$`_{des}$ and n reported

herein are composed of at least three absolute desorption rate constants and orders of reaction from ligand exchange reactions with phosphate at pH 7, and over the time scale of our measurements.

4.4 Adsorption Kinetics of Phosphate as DMA and Arsenate Desorbs:

4.4.1 Kinetic Curves

Phosphate adsorption kinetic parameters were calculated from spectra collected during DMA desorption experiments using different concentrations of phosphate. The left panel of Figure 16, shows representative time-dependent ATR-FTIR spectra of PO_4(ads) on DMA(ads)/α-Fe_2O_3 and DMA(ads)/α-FeOOH. Phosphate adsorption on freshly-prepared films, control experiments, shows identical spectral components in the range $1300 - 900$ cm^{-1}. Studies have found that the location and intensity of the observed spectral features vary with pH, degree of protonation of surface complexes, degree and strength of hydrogen bonding to neighboring sites, surface loading, data acquisition technique, and substrate characteristics (75). Under high surface loading of phosphate and near neutral conditions, similar to those used herein, deprotonated bidentate and monoprotonated monodentate surface phosphate complexes result in calculated IR frequencies with excellent correlation with experimental data on hematite and 2-line ferrihydrite (77, 78). It must be emphasized however, that given the structural differences in nature of sites of hydrated iron oxides and hydroxides, the intensities of these spectral components will vary even if surface loading and solution pH is the same.

For example, spectra shown for adsorbed phosphate on hematite in Figure 16 (near neutral pH and monolayer surface coverage) resemble those in Figure 5 reported by Elzinga and Sparks at pH 6.1 and pD 6.2 for high phosphate loading (75). More specifically, the most intense feature under these conditions is around 1100 cm^{-1}, followed by two overlapping features between 1000 and 1050 cm^{-1}. The weakest feature in intensity is located between 900 and 950 cm^{-1}. While goethite and ferrihydrite are structurally different, the spectra shown for phosphate adsorbed on goethite in Figure 16 resemble that shown in Figure 5 of Arai and Sparks (78). Again, these spectra were collected in-situ under high surface phosphate loading and near neutral pH. In their study, the most intense feature is between 1025 and 1050 cm^{-1} followed by a feature at 1075 and 1100 cm^{-1} and a third between 950 and 975 cm^{-1}. Figure 16 shows an intense feature at 1041 cm^{-1} followed by a second at 1084 cm^{-1} and a third at ~945 cm^{-1} (not labeled). Spectra reported by Persson *et al.*(80) were collected using solid samples of goethite with adsorbed phosphate, and hence can not be used for comparison with our spectra due to differences in the degree of sample hydration. As shown below, the growth of these labeled features as a function of time was used to quantify the kinetics of phosphate adsorption as a function of spectral components.

The right panel of Figure 16 shows adsorption kinetic curves of phosphate generated from the spectra shown in the left panel. Similar curves were obtained from experiments conducted at 1 mL/min flow rate of HPO_4^{2-}(aq). These curves were obtained from the baseline-corrected ATR absorbance [$A(\nu)$] of the spectral component at 1049 and 1041 cm^{-1} on α-Fe_2O_3 and α-FeOOH films, respectively. The baseline correction was

relative to the absorbance at 2000 cm^{-1}, which has no absorption from any of the species used.
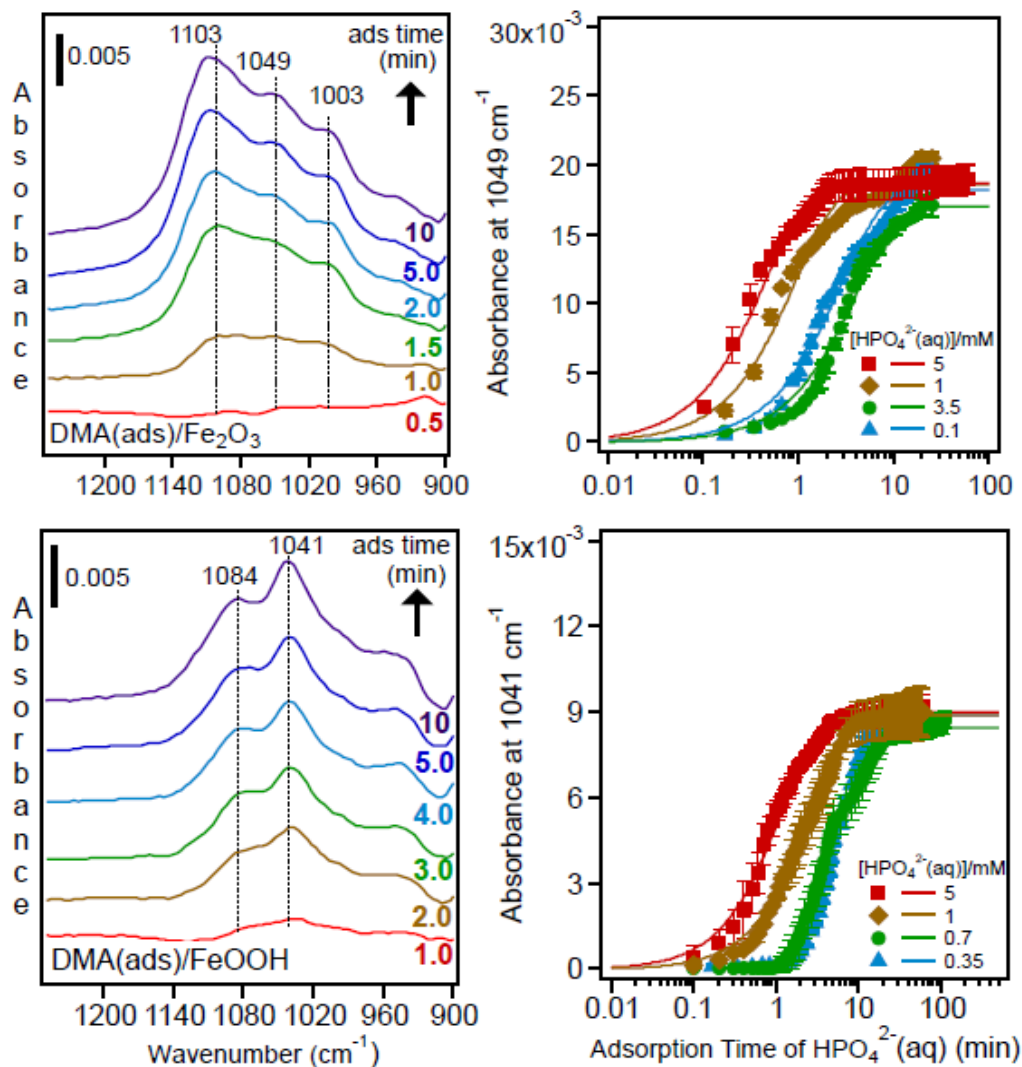
Figure 16. ATR-FTIR absorption spectra and adsorption kinetic curves collected as a function of time for the adsorption of 10^{-3} M HPO$_4^{2-}$(aq) on α-Fe$_2$O$_3$ (6 mg film, upper panel) and FeOOH (16 mg film, lower panel) respectively. These films were previously exposed to 0.5 mM DMA(aq) at pH 7 and 2 mL/min flow rate. For kinetic curves, markers and lines represent experimental data and least squares fit using the Langmuir adsorption kinetic model, respectively.

58

To extract apparent (and initial) adsorption rates from these experimental data, we used the simple first order Langmuir adsorption kinetic model used for DMA , where $\theta(t)$ is the relative surface coverage of $PO_4(ads)$, and b is a collection of constants that equal $k_{ads}[HPO_4^{2-}(aq)] / r_{obs}$. The apparent rate of phosphate adsorption, r_{obs}, is related to the adsorption and desorption rate constants: $r_{obs} = k_{ads}[HPO_4^{2-}(aq)] + k_{des}$. Figure 16 shows the fitted experimental data in the right panel. The linear form of this model is: $\ln(1-A(\nu)/b') = -r_{obs}t$. Values of b' were obtained by averaging data points in the plateau region. Values of r_{obs} were obtained from linear-least squares fits to the experimental data plotted in the linear form for the initial times of adsorption ($t < 5$ min). These values are listed in Table 7 and 8 as a function of film type.

Table 7. Phosphate adsorption kinetics on α-Fe_2O_3 surfaces as a function of spectral components from best fit parameters of least squares fits r_{obs} versus $[HPO_4^{2-}$ (aq)] data collected using 2 mL/min flow rate.

Spectral Component (cm^{-1})	Films with DMA(ads)			
	k_{ads} (min^{-1}M^{-1})	k_{des} (min^{-1})	K_{eq} (M^{-1})	$\log K_{eq}$[a]
1003	443 (20)	0.4 (0.1)	1108 (332)	5 (2)
1049	265 (13)	0.4 (0.1)	663 (200)	5 (2)
1103	409 (20)	0.4 (0.1)	1023 (307)	5 (2)
	Films with iAs(ads)			
1003	70 (4)	0.1 (0.03)	700 (200)	5 (2)
1045	48 (3)	0.07 (0.02)	686 (200)	5 (2)
1110	61 (3)	0.1 (0.03)	610 (200)	5 (2)
	Freshly-prepared films			
1003	365 (15)	0.2 (0.06)	1825 (600)	5 (2)
1049	488 (20)	0.3 (0.1)	1627 (400)	5 (2)
1103	385 (16)	0.1 (0.03)	3850 (1000)	5 (2)

Table 8. Phosphate adsorption kinetics on α-FeOOH surfaces as a function of spectral components from best fit parameters of linear least squares fits to r_{obs} versus $[HPO_4^{2-}(aq)]$ data collected using 2 mL/min flow rate.

Spectral Component (cm^{-1})	Films with DMA(ads)			
	k_{ads} (min^{-1}M^{-1})	k_{des} (min^{-1})	K_{eq} (M^{-1})	$logK_{eq}$[a]
1041	151 (10)	0.1 (0.05)	1678 (1200)	5 (3)
1084	96 (20)	0.1 (0.05)	960 (250)	5 (3)
	Freshly-prepared films			
1041	178 (2)	0.04 (0.02)	4450 (3000)	5 (3)
1084	116 (6)	0.01 (0.005)	11600 (6000)	6 (3)

The first order Langmuir adsorption kinetic model predicts a linear dependency of r_{obs} on $[HPO_4^{2-}(aq)]$ as shown in Figure 17 for phosphate adsorption on hematite and goethite films in the presence and absence of DMA(ads) using data from the 1049 and 1041 cm^{-1} kinetic curves, respectively. Studies were conducted as a function of flow rate using 1and 2 mL/min for hematite films. The lines through the experimental data are linear-least squares fit to the experimental data and best fit parameters, k_{ads} and k_{des}, are listed in Table 7. Because the x-axis is a logarithmic scale, the lines appear as curves. Values of k_{ads} from studies conducted using 1 mL/min flow rate are lower than those from studies conducted using 2 mL/min flow rate on hematite films suggesting more diffusion contribution to r_{obs}. Experiments at higher flow rates (> 2 mL/min) would result in mechanically removing the film from the ATR-FTIR crystal during the data collection time. From this observation, experiments on goethite were conducted using 2 mL/min flow rate only. The uncertainties in the values of k_{des} (y-intercepts) are higher than k_{ads} (slopes), which were propagated from the uncertainties in the values of r_{obs}.

For comparison, phosphate adsorption kinetic experiments were conducted on α-Fe_2O_3 with a monolayer of adsorbed arsenate, iAs(ads), at pH 7 and 2 mL/min flow rate. Representative time-dependent ATR-FTIR spectra are shown in Figure 18 in the spectral range 1300-700 cm^{-1} containing $v_3(PO_4)$ and $v(AsO_4)$ of surface phosphate and arsenate, respectively. Phosphate adsorption kinetic curves were generated from the baseline-corrected height of the spectral features labeled in Figure 18 located at 1003, 1045, and 1110 cm^{-1}. Values of r_{obs} were obtained from the linear least-squares fits to experimental data plotted in the linear form of the Langmuir model described above.
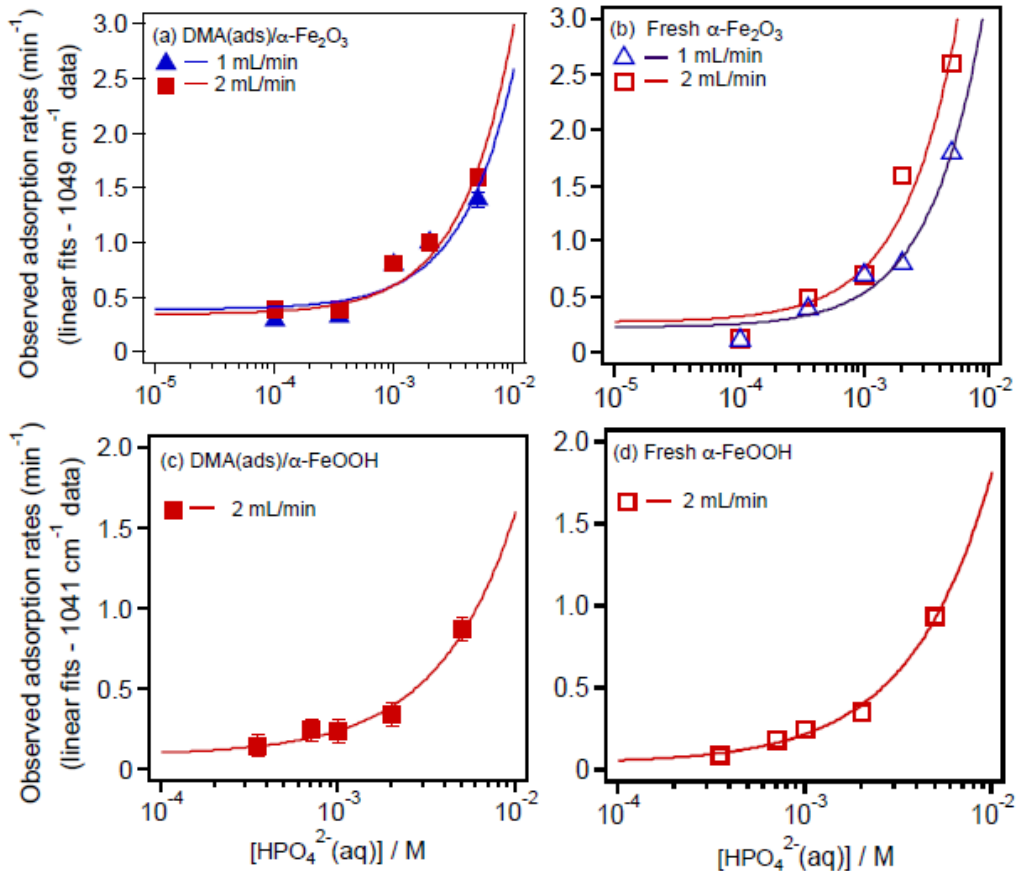
Figure 17. Dependency of apparent phosphate adsorption rate constants, r_{obs}, on the concentration of $[HPO_4^{2-}(aq)]$. Lines through the data represent linear least squares fits. Best fit parameters are listed in Table 7.
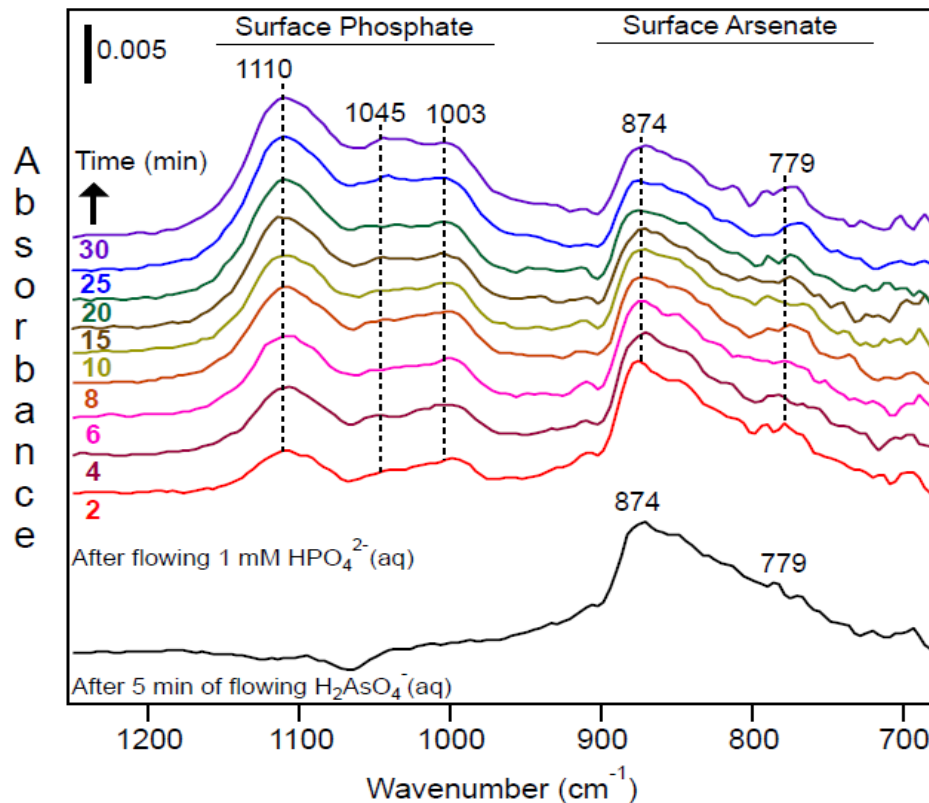
Figure 18. Representative ATR-FTIR absorptions spectra collected as a function of time for the adsorption of 10^{-3} M HPO_4^{2-} (aq) on iAs(V)/α-Fe_2O_3 film (6 mg film, 2 mL/min flow rate) at pH 7.

Figure 19 shows the linear dependency of r_{obs} on [HPO_4^{2-}(aq)] and best fit parameters are listed in Table 7 from the kinetic curves of the spectral feature at 1110 cm^{-1}. The trend observed from the values of k_{ads} shows that phosphate adsorption kinetics through ligand exchange depends on the type of the leaving groups.
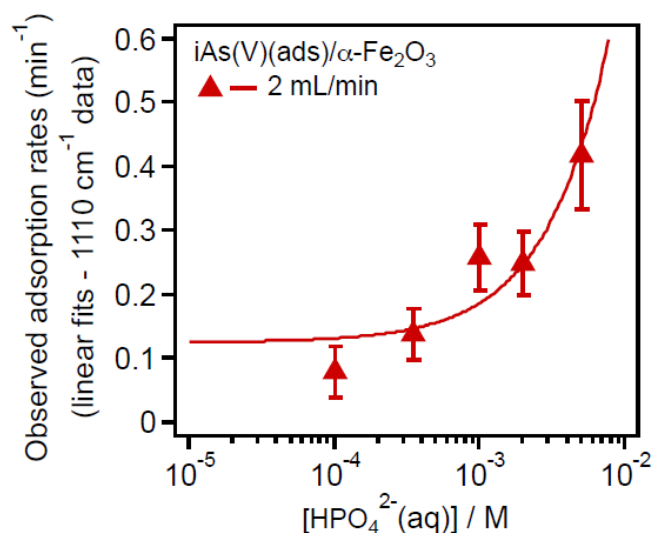
Figure 19. Dependency of apparent HPO_4^{2-} (aq) adsorption rate constants, r_{obs} on the concentration of [P(V)-aq] from studies conducted on iAs(V)(ads)/α-Fe$_2$O$_3$ films (6 mg) at pH 7 and 2 mL/min flow rate. Adsorbed arsenate was introduced initially by flowing 0.5 mM aqueous $HAsO_4^{2-}$ (aq). Lines through the data represent linear least squares fits. Best fit parameters are listed in Table 7.

In general and taking into account the uncertainties in the values of k_{ads}, the highest values of k_{ads} (and hence the fastest phosphate adsorption kinetics) are observed on freshly-prepared Fe-(oxyhydr)oxide films and those with nearly monolayer coverage of DMA(ads) from the kinetic behavior of spectral components at 1003 and 1110 cm^{-1} for hematite, and 1041 and 1084 cm^{-1} for goethite. The lowest value of k_{ads} (and hence slowest phosphate adsorption kinetics) are observed on hematite films with nearly monolayer coverage of iAs(ads). The kinetic behavior of the spectral component at 1045 cm^{-1} on hematite yielded k_{ads} values that increase in this order: arsenate-covered < DMA-covered < freshly-prepared. As stated above, the spectral features observed

experimentally for adsorbed phosphate were assigned to deprotonated bidentate and monoprotonated monodentate complexes. For a given arsenic-covered hematite film (i.e. DMA-covered or arsenate-covered), the similarity in the kinetic behavior of the two spectral components at 1003 and 1110 cm^{-1} suggest that they originate from the same type of surface complex. By comparison, the kinetic behavior of the spectral component at 1045 cm^{-1} show values of k_{ads} that are lower by a factor of 2 on arsenic-covered hematite films. This suggests that the phosphate complex characterized by the 1045 cm^{-1} forms as a result of a ligand exchange process with a strongly-bonded DMA(ads) or arsenate(ads). However, on a freshly-prepared hematite film, the opposite trend is observed, where the kinetic behavior of the spectral component at 1045 cm^{-1} show values of k_{ads} that are slightly higher by a factor of 1.3. Since under neutral conditions (below the point of zero charge (PZC) of freshly-prepared hematite), the relative population of $-FeOH_2^+$ sites is relatively higher than $-FeOH$ groups with a low likelihood of finding two adjacent protonated sites, the above observation suggest that the 1045 cm^{-1} might be arising mostly from the monoprotonated monodentate phosphate complex. For data shown in Table 8 on goethite films, the similarities in the kinetic behavior of the spectral components analyzed for phosphate adsorption on DMA-covered and freshly-prepared films suggest that they originate from the same type of surface complexes. Comparing values of k_{ads} between hematite and goethite is not straight forward because these rates are not corrected for geometrical differences in the shape of the particles (spherical versus needle-shaped) or the density of deposited films, which are factors that impact kinetics of surface interactions.

Values of pseudo rate constants obtained from these surface-sensitive kinetic measurements can be used to calculate the binding constant at equilibrium, K_{eq}, according to this relation: $K_{eq} = k_{ads}/k_{des}$. Values of K_{eq} and $logK_{eq}$ are listed in Tables 7 and 8 along with uncertainties propagated from errors associated with k_{ads} and k_{des} values. The results clearly show that while values of k_{ads} of phosphate are lower by a factor of $1 - 2$ and $6 - 8$ on DMA- and arsenate covered hematite surfaces at 2 mL/min, respectively, relative to freshly-prepare films, values of K_{eq} are identical among these different films. This observation is consistent with chemical intuition that predicts the fastest ligand exchange process to take place between HPO_4^{2-}(aq) and surface water followed by DMA(ads) and iAs(ads). While both DMA(ads) and iAs(ads) form simultaneously inner- and outer-sphere complexes, the trend in the values of phosphate k_{ads} clearly suggests that DMA(ads) exists mostly in outer-sphere or monodentate complexes, whereas iAs(ads) exists mostly in strongly-bonded bidentate complexes. This suggests that fast kinetic studies that probe the adsorption behavior during initial times of surface interactions are better than those conducted at equilibrium in delineating molecular level differences among different surfaces.

Figure 18 shows a broad absorbance feature with the most intense absorbance at 874 cm^{-1} due to arsenate surface complexes on hematite. Upon flowing HPO_4^{2-}(aq), a reduction in the overall intensity band is observed, and a feature at 779 cm^{-1} becomes more pronounced. The IR signature of adsorbed arsenate has been studied extensively at equilibrium on a number of metal-(oxyhydr)oxides that include hematite and goethite (61, 62, 64-66, 81, 84, 85). These studies coupled with results from x-ray absorption studies reported that arsenate forms predominantly inner-sphere bidentate binuclear

complexes, which gives rise to v(As-O-Fe) in the range 824-800 cm^{-1} (64-66). The

formation of inner-sphere monodentate complexes involved in hydrogen bonding with

neighboring sites was also reported as a function of pH (72). Values of v(As-O) in these

complexes range from 860-780 cm^{-1} for singly protonated monodentate complexes

around neutral pH, and from 885-810 cm^{-1} for doubly protonated monodentate complexes

under acidic pH (less than 3). The lowest frequency is assigned to v(As-OH) in these

protonated complexes, which is in general weaker in intensity than features located ≥ 800

cm^{-1}. Simultaneous formation of inner- and outer-sphere complexes of adsorbed arsenate

was reported by Catalano *et al.* at pH 5, where the latter can give rise to v(As-O) in the

range 861-854 cm^{-1} due to weak interactions with –FeOH sites (45). In light of these

studies, and given the data shown in Figure 18 under neutral pH (lower than PZC of

hematite, with a higher aqueous concentration of $HAsO_4^{2-}$ than $H_2AsO_4^{-1}$), over the time

frame of our measurements, arsenate forms a mixture of mono- and bidentate inner-

sphere protonated complexes giving rise to v(As-OH) at 779 cm^{-1} (too low in frequency

to be assigned to v(As-O-Fe) according to Myneni *et al*, and a broad absorption in the

range 800 – 900 cm^{-1} composed on a number of overlapping bands (56, 81). The latter

feature contains absorptions assigned to v(As-OFe), uncomplexed v(As-O) with a bond

order of 1.5 due to resonance, or v(As-O) weakly H-bonded to neighboring –FeOH sites.

The spectra in Figure 18 also shows that upon flowing phosphate, the feature at 779 cm^{-1}

persists suggesting that it is very likely due to the presence of a protonated bidentate

complex. The formation of outer-sphere complexes can not be excluded, and the

reduction in the intensity of the 875 cm^{-1} might be interpreted as evidence for their

presence on the surface under our experimental conditions as suggested by Roddick-Lanzilotta *et al* (86).

Kinetic curves were generated by plotting the baseline-corrected heights of the absorbances at 874 cm^{-1} characteristic of iAs(ads). To extract pseudo desorption rate constants, experimental data were plotted in the linear form of the desorption Langmuir model, $\ln\left(\dfrac{\theta(t)}{\theta_0}\right) = -k'_{des} \cdot t$ where $\theta(t)$ is the absorbance at a given ν, θ_0 is the maximum absorbance before desorption starts, and k'$_{des}$ is the initial desorption rate constant that equals $k_{des}[HPO_4^{2-}(aq)]^n$, where n is the order of desorption. The dependency of k'$_{des}$ on $[HPO_4^{2-}(aq)]$ is shown in Figure 20 for DMA and arsenate desorption from hematite surfaces. More phosphate concentrations were tested as compared to the DMA data shown in Figure 17 and 18 for better and more precise comparison to arsenate results. The results show that under our experimental conditions using $[HPO_4^{2-}(aq)]$ in the range 10^{-4} - 5×10^{-3} M, an order of n=1 produces an excellent fit to the DMA data. For the arsenate desorption case, an order of n=0.6 produces a better fit than n=1. Overall, it is clear that DMA desorbs faster by a factor of nearly 7 than arsenate using phosphate as a desorbing agent. These results support the interpretation above that the proportion of outer-sphere and monodentate DMA complexes on hematite is larger than bidentate complexes, and that arsenate exists mostly as strongly-bonded bidentate.
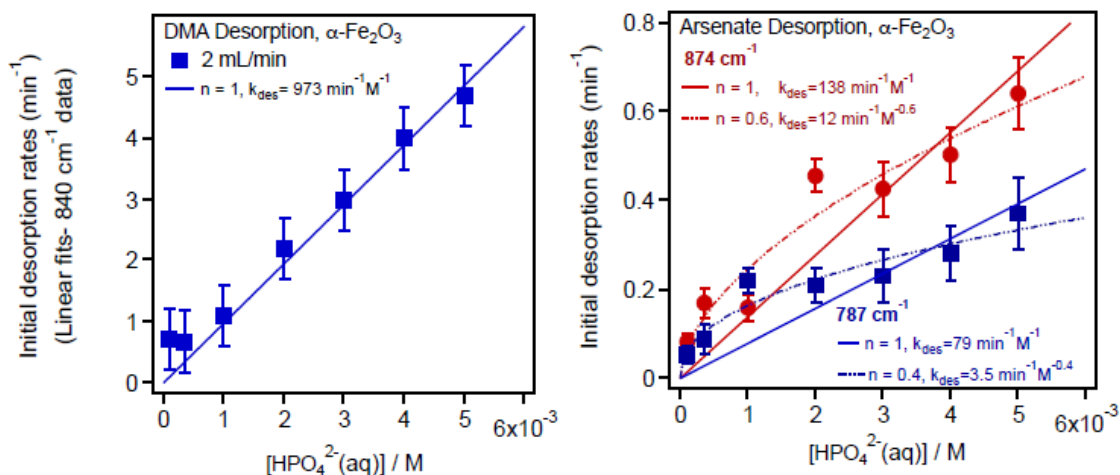
Figure 20. Dependency of initial desorption rates of surface DMA and arsenate on the concentration of [HPO_4^{2-}(aq)] from studies conducted using α-Fe_2O_3 films (6 mg) at pH 7 and 2mL/min flow rate. Both adsorbed DMA and arsenate were introduced by flowing 0.5 mM aqueous solutions at pH 7 and I = 0.01 M KCl. Lines through the data represent linear least squares fits. Best fit parameters are listed in the inset.

To provide further evidence for the existence of more bidentate complexes of iAs(ads) than DMA(ads), the adsorption kinetics of $H_2AsO_4^-$(aq) on hematite was studied using ATR-FTIR as a function of [$H_2AsO_4^-$] at pH 7, I = 0.01 M KCl and 1 mL/min flow rate. Adsorption kinetic curves were generated from the base-line corrected height at 874 cm^{-1} and data were analyzed in a similar fashion described above for the case of DMA and HPO_4^{2-}(aq). Figure 21 shows the dependency of r_{obs} on [$H_2AsO_4^-$(aq)] with best fit parameters, k_{ads} and k_{des} at 788 $M^{-1}min^{-1}$ and 0.07 min^{-1}, respectively. When these values are compared those for DMA (400 $M^{-1}min^{-1}$ and 0.3 min^{-1}), it is clear that the adsorption kinetics of arsenate are higher than those of DMA. This result is predicted from the thermodynamic measurements of the binding affinities of these compounds (47, 48).

68
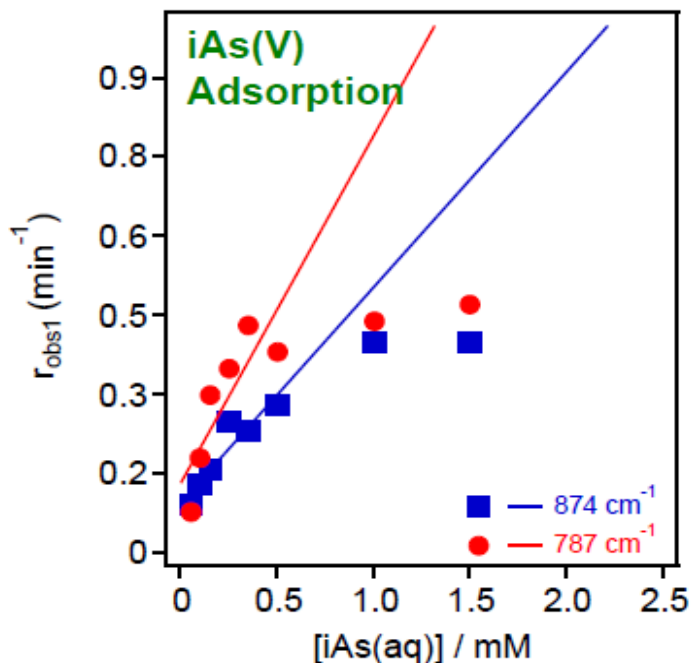
Figure 21. Dependency of apparent $H_2AsO_4^-$ adsorption rate constants, r_{obs} on $[H_2AsO_4^-$ (aq)] from studies conducted on α-Fe_2O_3 films (6 mg) at pH 7 and 1 mL/min flow rate. The line through the data represents the linear least squares fit. Best fit parameters are: slope = 788 $M^{-1}min^{-1}$ and y-intercept = 0.07 min^{-1}.

Figure 22 shows adsorption isotherms of a) DMA and b) arsenate obtained from the plateau of kinetic curves generated from the most intense spectral components 840 and 875 cm^{-1} respectively, after reaching equilibrium.
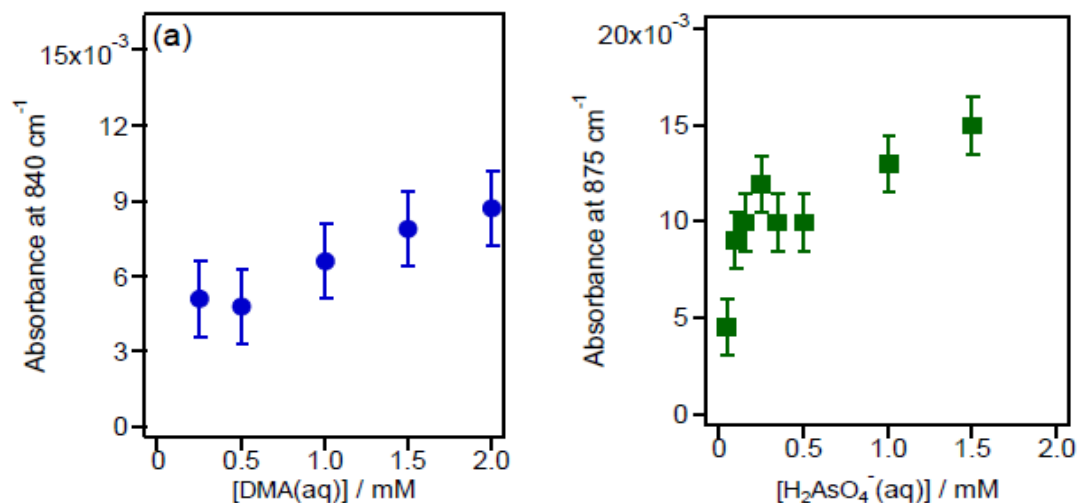
Figure 22. Adsorption isotherm of a) DMA and b) arsenate on freshly-prepared α-Fe_2O_3 (6 mg films, pH 7, $I = 0.01$ M KCl) obtained from the plateau of kinetic curves of the most intense spectral components 840 and 875 cm^{-1}, respectively, after reaching equilibrium.

To contrast our results with previous EXAFS studies discussed above, the analysis herein suggests that the presence of two methyl groups on arsenate instead of oxygen does not dramatically lengthen the As-Fe interatomic distances. However, it is reported that increasing organic substitution on arsenate results in lower binding affinity of disubstituted DMA than arsenate to Fe- and Al-(oxhydr)oxides by 1-2 orders of magnitude at pH 7 (58, 59). In light of the data analysis presented in this thesis, integrated analysis of structural, thermodynamic and kinetic analysis strongly suggests that increasing organic substitution (two methyl groups on DMA versus none on arsenate) reduces the protonation of strongly-bonded bidentate to relatively weaker monodentate and outersphere complexes.

Conclusions:

Results presented here are *in situ* and surface-sensitive ATR-FTIR rapid kinetic studies on the adsorption and desorption of DMA to/from α-Fe$_2$O$_3$ and α-FeOOH at pH 7 and I=0.01 M KCl. The adsorption kinetic data suggests fast and slow rates that are independent of the aqueous phase flow rates employed. Desorption experiments conducted using Cl$^-$(aq) and HPO$_4^{2-}$(aq) as desorbing agents were modeled using a modified Langmuir desorption model. Apparent desorption rate constants using HPO$_4^{2-}$(aq) were higher by 1-2 orders of magnitude than those using Cl$^-$(aq) and were found to depend on [HPO$_4^{2-}$(aq)] with an overall order of 0.3.

The results also suggest that under neutral solution conditions, the kinetics of ligand exchange reactions between aqueous phosphate is fastest on freshly-prepared films dominated by water surface groups. When DMA or arsenate are present on the surface near saturation coverage, the kinetics of the ligand exchange is faster with DMA(ads) than with iAs(ads). This observation, combined with analysis of the adsorption kinetics and structural data, strongly suggests that the proportion of weakly-bonded monodentate and/or outer-sphere DMA(ads) complexes is higher than those formed by iAs(ads) that exist predominantly in the bidentate configuration. Hence, under neutral conditions with relatively high Fe and P conditions, DMA becomes mobilized, and readily bioaccessible for uptake and recycling to other forms of arsenic. In technologies aimed at lowering the arsenic content in organic-rich fuels or industrial waste water, introducing Fe-(oxyhdr)oxides in a form that maximizes contact with the contaminated media would be an efficient procedure. However, careful analysis has to be done to the type of stable

species that co-exist with arsenic compounds, particularly those such as P that have the same or higher affinities to compete for sites on the Fe-containing removal media.

These results are significant as they constitute systematic *in situ* kinetic investigations of DMA surface interactions with α-Fe$_2$O$_3$ and α-FeOOH using the surface sensitive technique ATR-FTIR. Because DMA forms simultaneously inner- and outer-sphere surface complexes on Fe-(oxyhydr)oxides, the mechanism of the surface chemistry of DMA is complex at the molecular level. While the empirical Langmuir adsorption and desorption models were used to model the experimental data at a single pH and ionic strength, these studies highlight the need for developing time-dependent surface complexation models that take into account surface charge, pH and ionic strength of the phase. Also, the ability of HPO$_4^{2-}$(aq) to release adsorbed DMA under neutral conditions using concentrations as low as 3 mg/L P further supports other studies on DMA that found it to be a more mobile and more bioavailable organoarsenical than MMA or arsenate. When combined with our understanding of its high affinity to Al/Fe (oxyhyr)oxides, DMA will potentially be released and converted to the more toxic and less mobile forms of arsenic in the presence of efficient desorbing agents. In the absence of the latter, DMA will most likely be localized, and –over time- will form the thermodynamically more stable inner-sphere bidentate complexes. With this analysis of the surface chemistry mechanism of DMA by Fe-(oxyhyr)oxides, mathematical models of its fate in iron-rich soils, and the design of cleanup adsorbents used in remediating contaminated soils or reducing arsenic content in fuels can be designed.

Appendix A: From Single Beam to Absorbance Spectra in OMNIC

Infrared (IR) spectroscopy measures the infrared intensity versus wavelength (wavenumber) of light. It detects the vibration characteristics of chemical functional groups in a sample. When an infrared light interacts with the sample, chemical bonds will stretch, contract, and bend. As a result, a chemical functional group tends to absorb infrared radiation in a specific wavenumber range regardless of the structure of the rest of the molecule. This way, the correlation of the band wavenumber position with the chemical structure is used to identify a functional group in a sample.
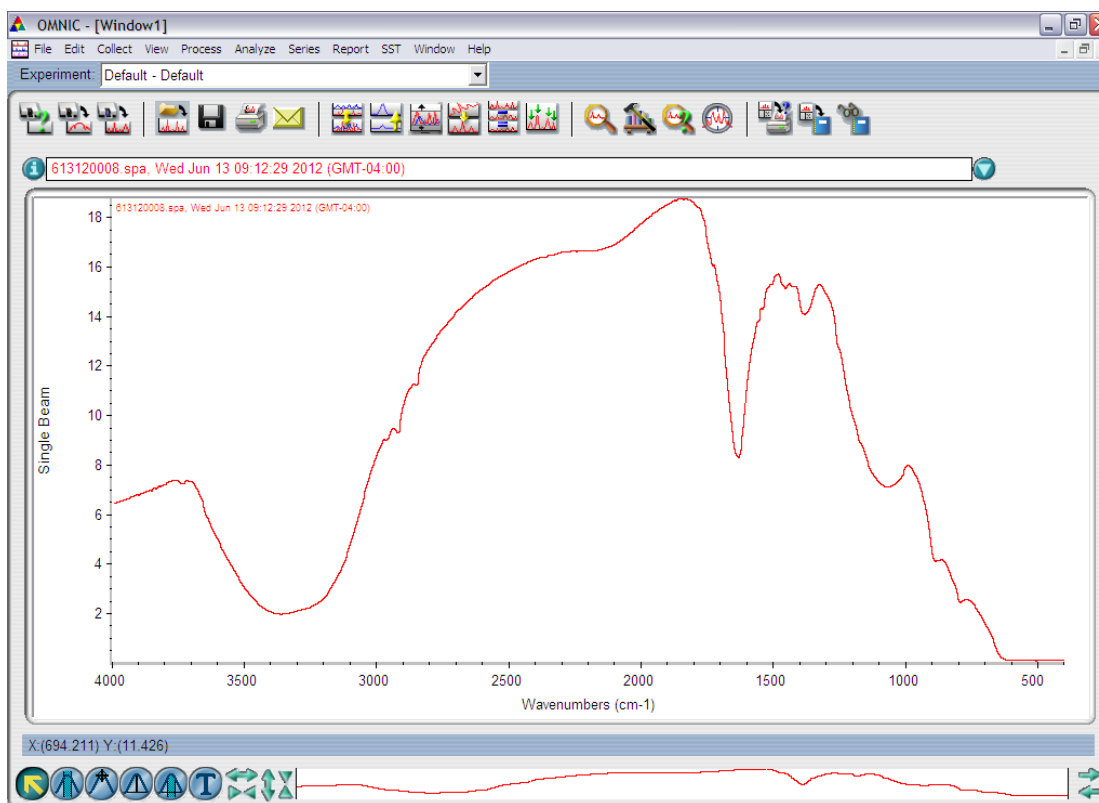
Figure A1. Single Beam spectrum in OMNIC.

A FTIR spectrometer obtains infrared spectra by first collecting an interferogram of a sample signal with an interferometer, which measures all infrared frequencies simultaneously. The spectrometer acquires and digitizes the interferogram, performs the FT function, and generates a single beam spectrum in the program OMNIC as shown in Figure A1. This spectrum is a plot of raw detector response versus wavenumber.

In any experiment, a spectrum of the dry film is first taken, followed by spectra of the background KCl solution at 90 min when the film has reached equilibrium, followed by adsorption and desorption spectra at certain time increments for up to 30-90 min. To collect spectra at small time increments, the number of averaged scans can be adjusted such that less time is needed for each spectrum. This is done by clicking on Experimental Setup under the Collect tab. Under No. of Scans, the value can be changed to adjust the time each spectrum takes to collect, such that more spectra can be obtained in a shorter time period. The Base Name can also be set in the form: ddmmyy such that all spectra are then saved in order, with the full name ddmmyyxxxx where xxxx ranges from 0001 to the total number of spectra collected in the experiment.
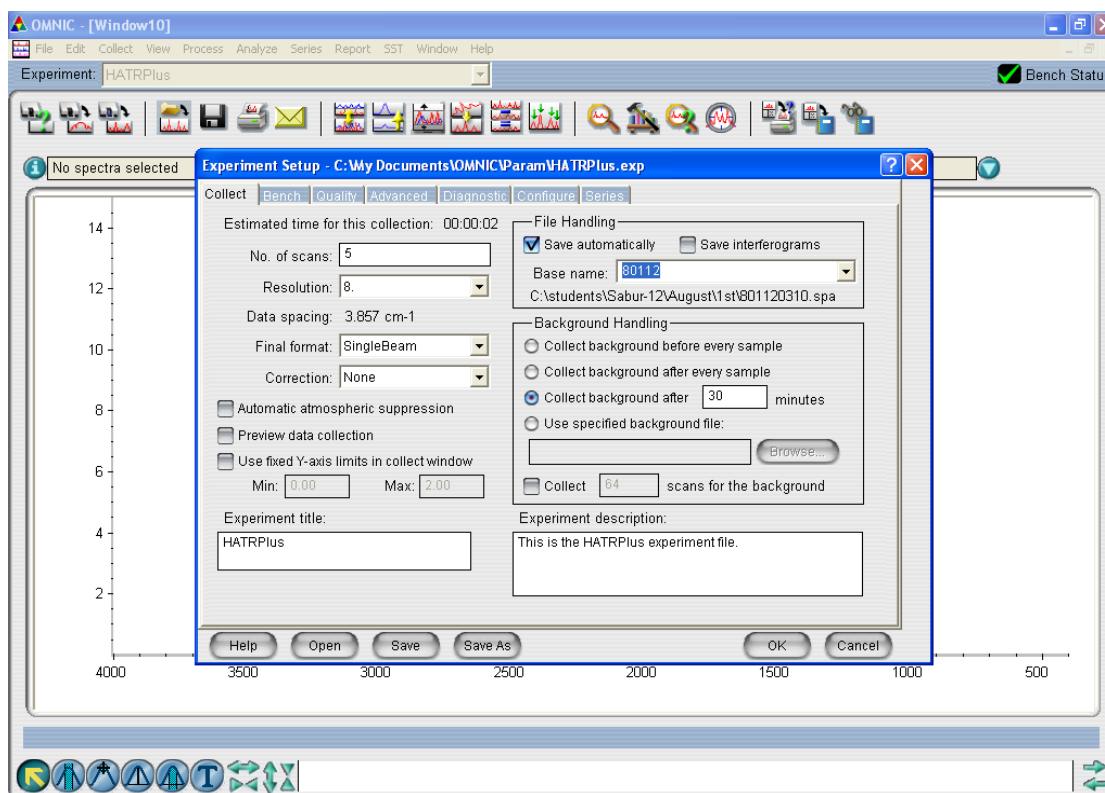
Figure A2. Experimental Setup window in OMNIC.

In order to obtain absorbance spectra, the single beam spectra obtained at different times are referenced to the background spectrum giving rise to plots which show bands due only to adsorbed or desorbed species. This is done by clicking on Reprocess under the Process tab.
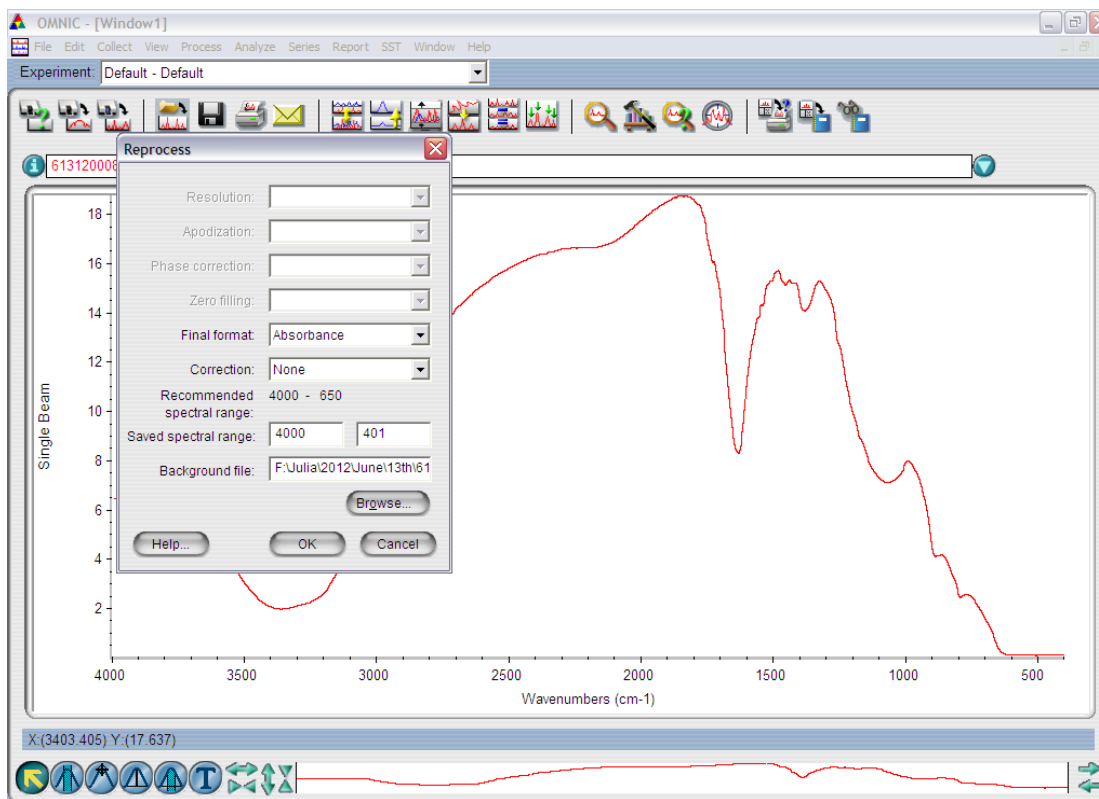
Figure A3. Reprocessing single beam spectra to absorbance spectra.

Under the Reprocess window, Absorbance is selected as the final format, and the respective KCl background file is entered. This will result in absorbance spectra showing bands due to the adsorbing species as shown below. The peak heights of the absorbance spectra are then measured using the peak height tool which is found in the bottom left corner of the screen. The baseline is adjusted such that one cursor is set in an area where nothing absorbs so that nothing interferes with the peak height and the second cursor is adjusted to form a straight baseline close to the peak being measured. The height is then given in the bottom left corner of the screen.
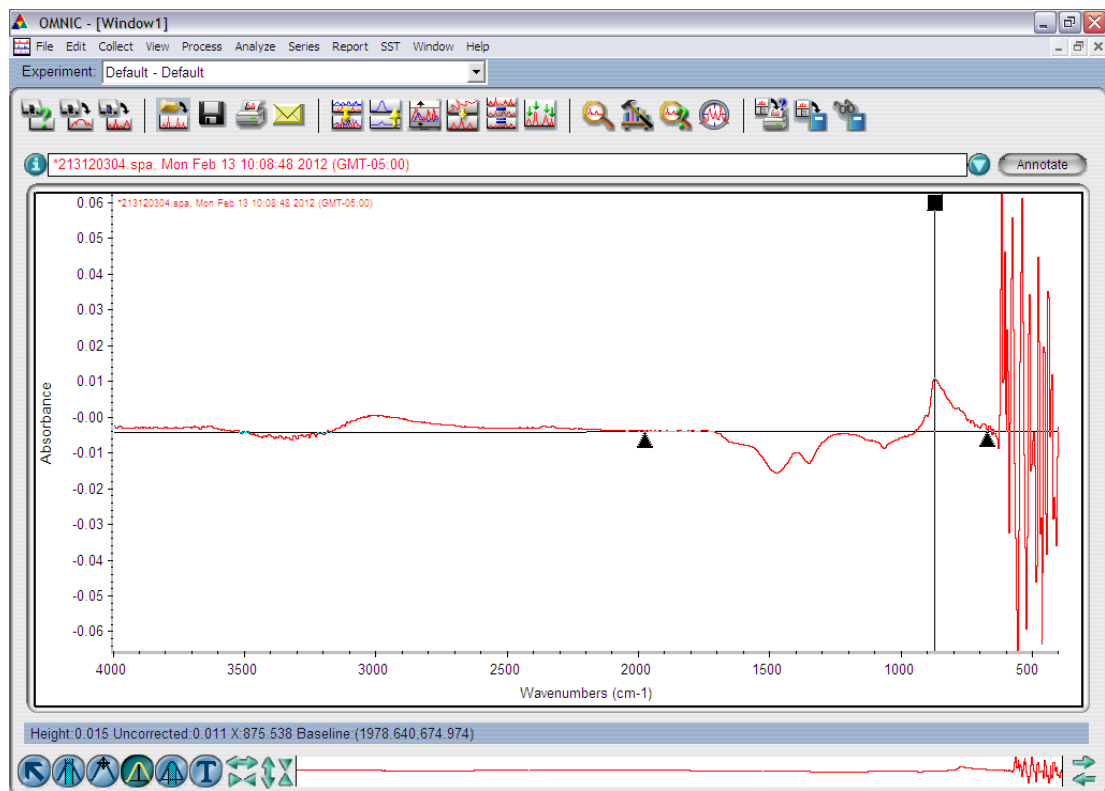
Figure A4. Measuring peak height in OMNIC of an absorbance spectra.

Appendix B: Collecting and Reprocessing Multiple Spectra by Macros Basic

In order to collect a higher number of spectra in a shorter period of time, Macros Basic can be used together with OMNIC. Macros Basic was programmed using different commands such that spectra are collected consecutively. The file used to do this was spectracollect shown below.
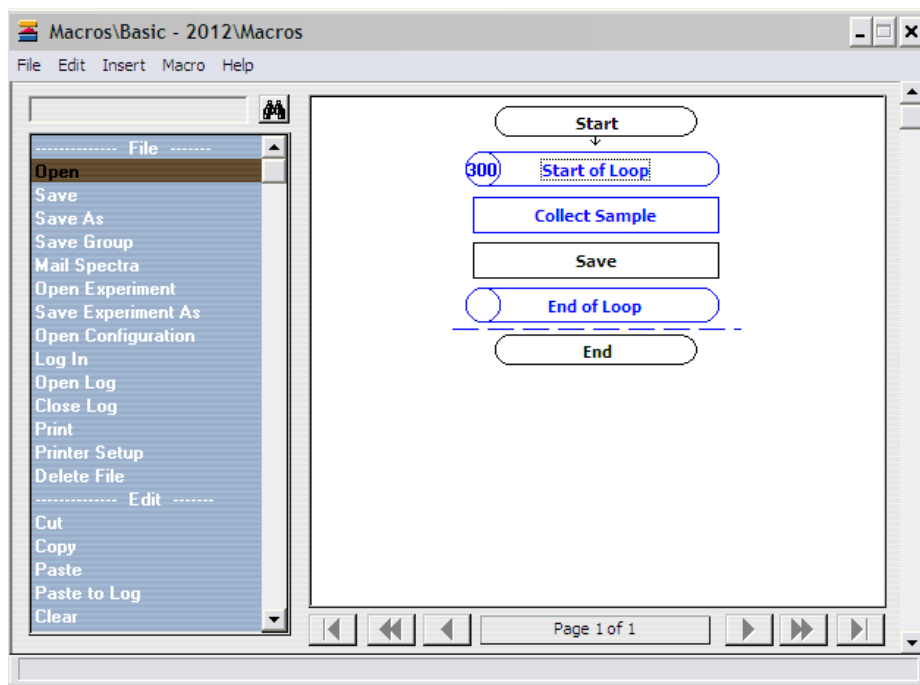
Figure B1. Spectracollect Macros Basic file used to collect multiple spectra consecutively.

The first command is the start of a loop of, in this case, 300 spectra. This value can be changed based on how long a different number of averaged scans takes to collect a spectrum. The second command starts the spectra collection followed by the second command of saving the spectra in the folders selected originally in OMNIC. The final command ends the loop and all the single beams collected are visible in one window in OMNIC.

In order to reprocess a large number of spectra, a different Macros Basic file is used, and shown below.
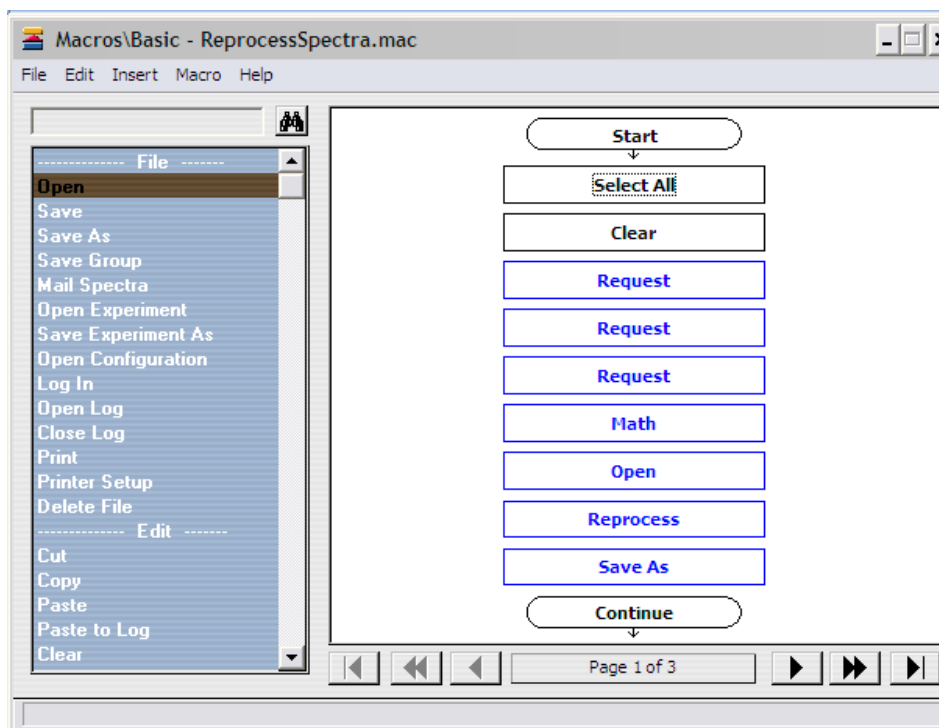
Figure B2. Macros Basic file used in reprocessing multiple spectra.

The first two commands, Select All and Clear, are in order to make sure the active window in OMNIC will be cleared of any spectra collected previously to starting the Macros. This is followed by 3 Request commands which are questions for to the user in order to obtain certain variables that will be used for the rest of the Macros. The first request, shown below, asks: What is the number of the first single beam spectra? This is for the Macros to know where to start the loop. The second request asks: How many spectra will be processed? This determines how many times the loop will be running through. The third request asks: What is the base name of the spectra? This is for the Macros to use the correct spectra files.
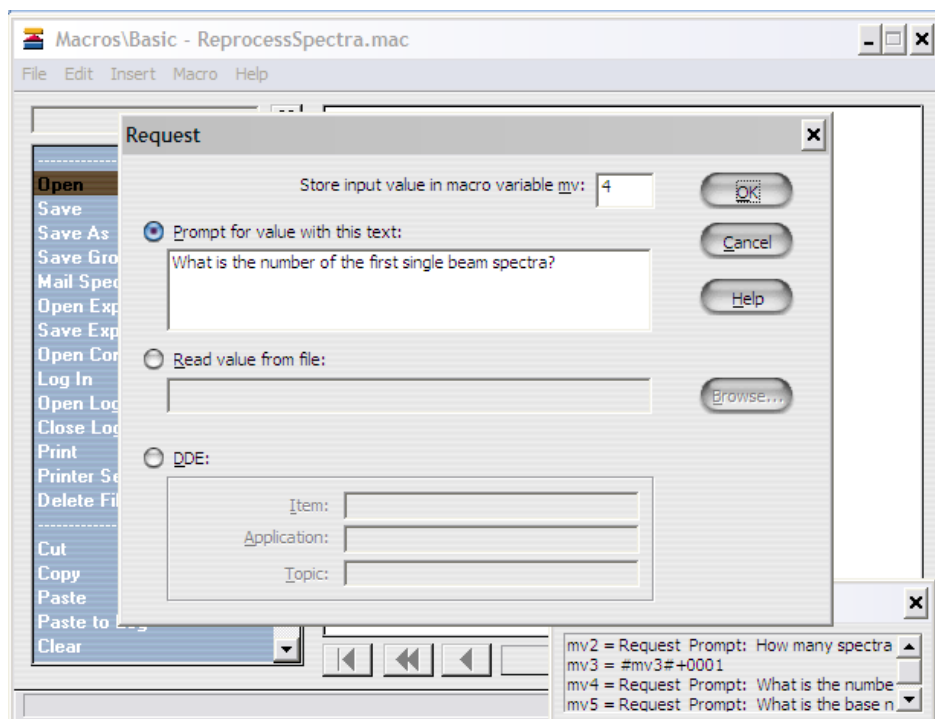
Figure B3. Request command.

The command following the requests is Math, shown below. This command puts the third Request and the first Request variables together such that the name of the spectra to be converted can be obtained in the format ddmmyyxxxx. This is now set as another variable.

Open is the following command and is shown below. This command uses the variable determined by Math to open the correct spectra for reprocessing. The folder the spectra are saved in must also be entered in order for the Macros to know where to find the spectra.
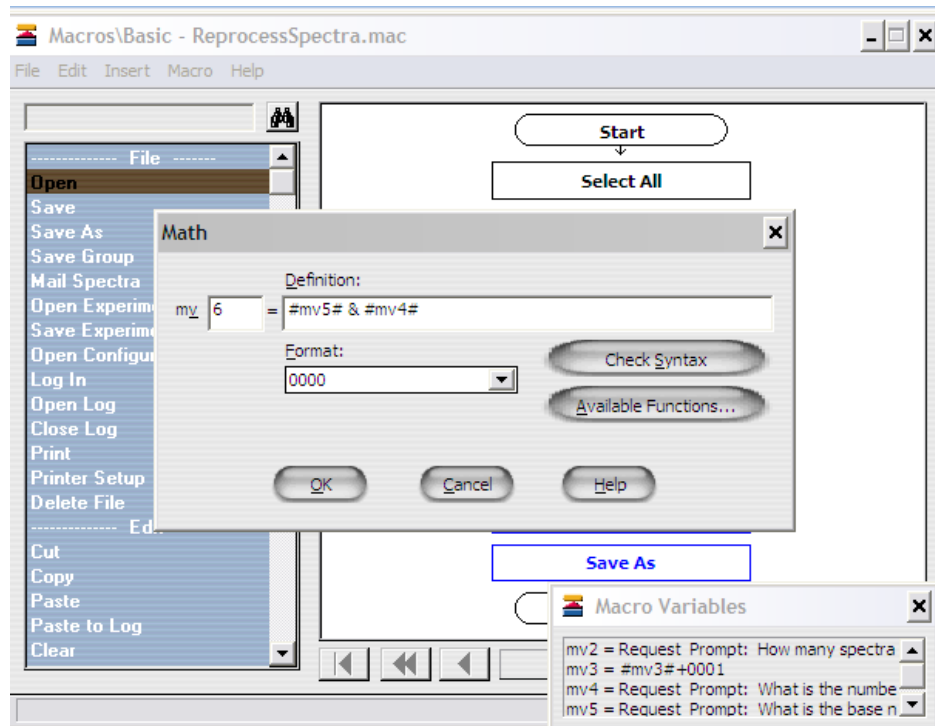
Figure B4. Math command.
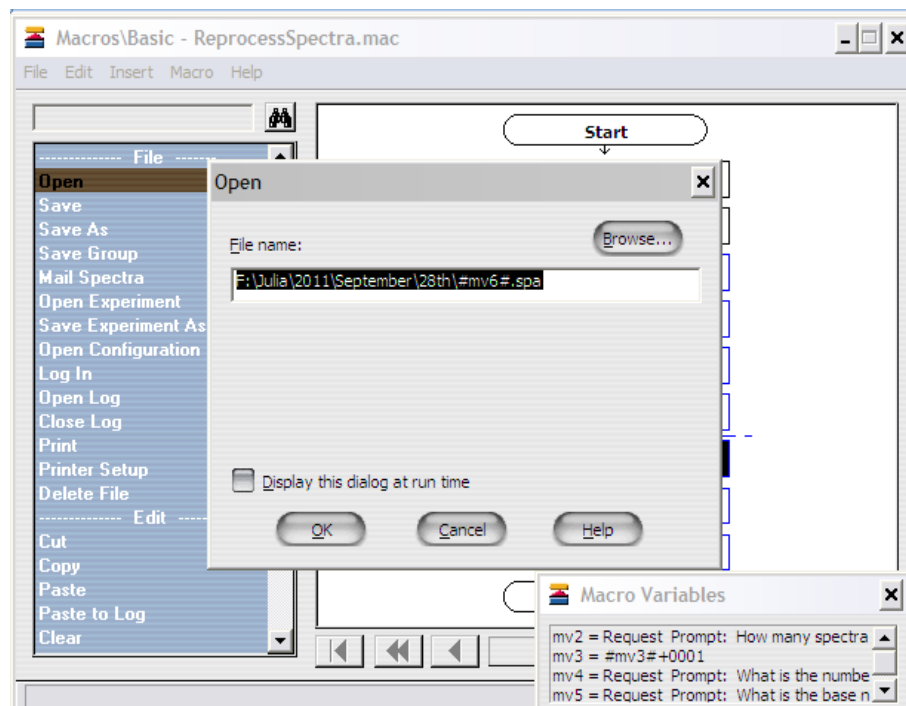
Figure B5. Open command in spectra reprocessing Macros.

The following command is Reprocess which the Macros uses in OMNIC as shown in Appendix A above. Once the spectrum is reprocessed, it must be saved under the Save As command. The command allows the user to select a folder that the spectra will be saved in and the Macros will use the same name as the corresponding single beam that the spectra was reprocessed from.

On page 2 of the Macros, the first command is a Math command, shown below, which determines the name of the following spectra to be reprocessed. A second Math command follows which subtracts 1 from the variable determined by the second Request command which determined the number of spectra that will be reprocessed in order for the Macros to move on to the next spectra.
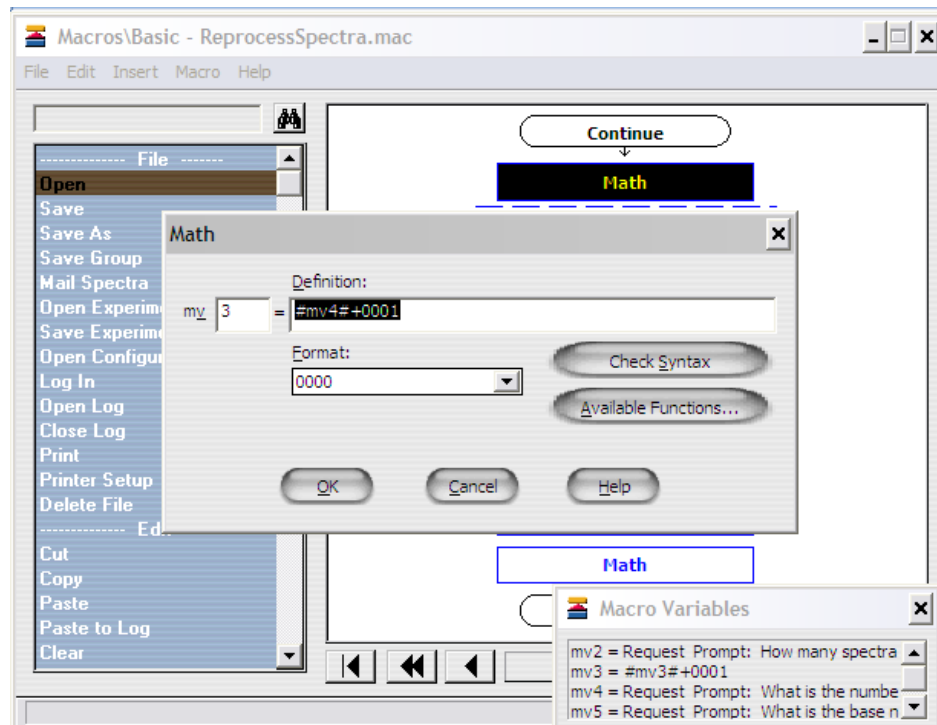
Figure B6. Math command.

The loop then begins using the last Math variable as the number of times it will loop through. The commands within the loop are the same as those on the first page of the Macros beginning with Math to determine the name of the spectra to be converted by the macros in the format ddmmyyxxxx increasing by the Math command shown in Figure B6. The respective spectra is then opened from the folder in the Open command followed by its conversion by the Reprocess command and saved in its corresponding folder as entered in the Save As command. The last Math command adds 0001 to the converted spectrum name such that the loop moves to the next spectrum. Once the second Request variable of how many spectra will be converted is complete, the loop ends.

Peak heights can also be measured for each spectrum using Macros by using the Peak Height command. This cuts down the amount of time required when running experiments that collect a large number of spectra.
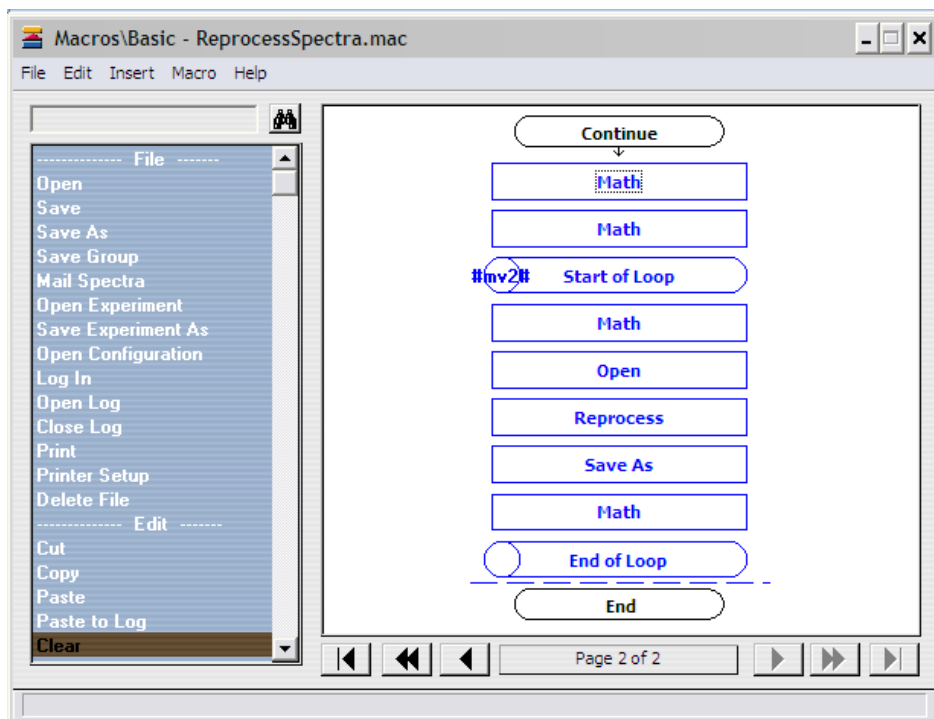
Figure B7. Page 2 of the ReprocessSpectra Macros.

Appendix C: Kinetic Curves and Data Analysis in IGOR

Once the peak heights have been measured, kinetic curves can be put together by plotting the peak absorbances as a function of time in IGOR. The time axes are determined based on the amount of time it took the Macros to collect all the spectra, which is also recorded while each spectrum is collected as part of the spectra name. The y and x axis are entered in and are called waves in IGOR.

In order to fit the kinetic curves with a certain equation, the cursors and tools must be activated by clicking on Show Info and Show Tools under the Graph tab. The cursors will show up at the bottom left corner of the graph while the different tools will show up at the top left corner of the graph. Cursor A is then placed on the first point of the curve while cursor B is placed on the last point. To select the fitting function, Curve Fitting must be selected under the Analysis tab. Under the Curve Fitting window, the first tab is Function and Data. This is where the fitting function can be selected or inserted if not available as one of the common functions. To insert a function, New Fit Function is selected. This will open a window where the variables of the function and the function itself can be typed out. Once the correct function is selected, the x and y axis is selected by clicking on the Y Data and X Data drop-down tabs. To select the range, the Data Options tab is selected, and Cursors is clicked, such that the range previously selected by the cursors is used as the fitting range. The Coefficients tab is then selected which allows the user to approximate the variables of the fitting functions. Under the Output Options tab, selecting X Range Full Width of Graph will ensure the fitting will range over the full length of the x axis. Once all of the above is selected, clicking Do It on the bottom left corner of the Curve Fitting window will fit the graph as selected by the user.
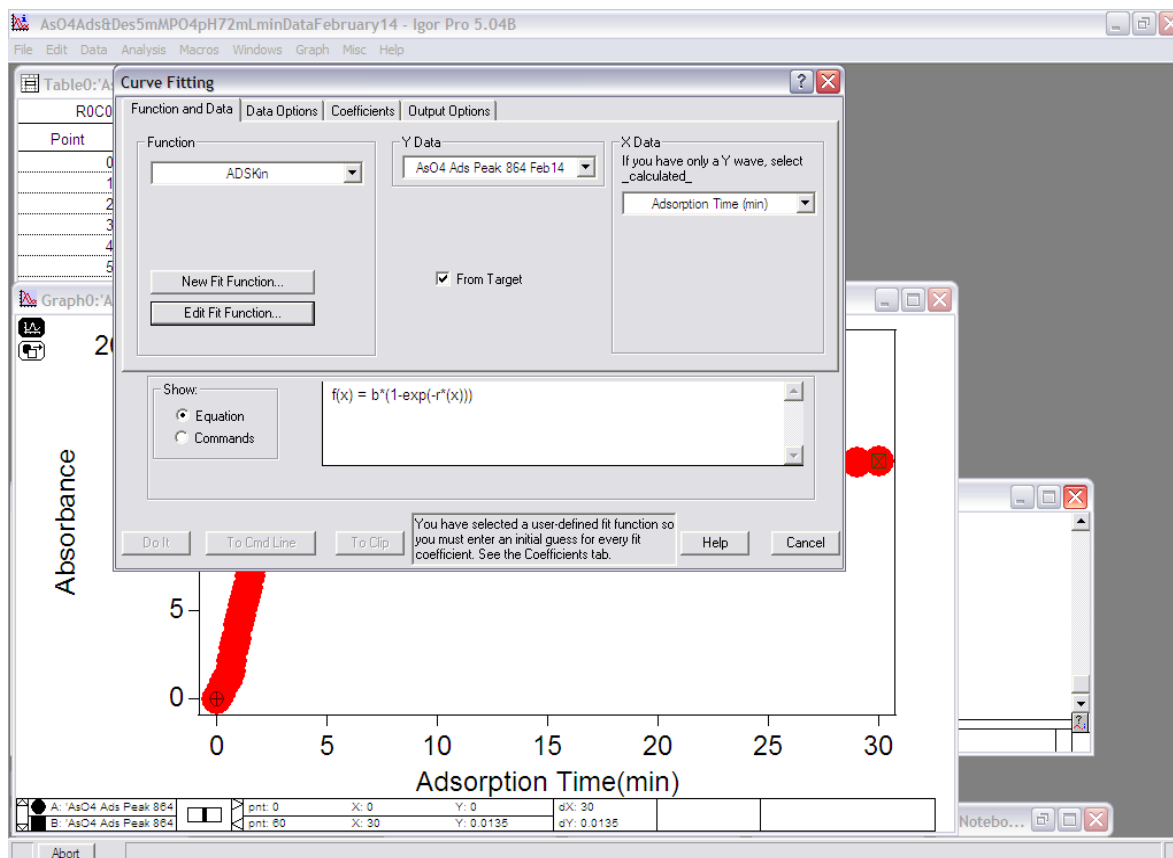
Figure C1. Curve fitting window.

In order to obtain our fitting parameters, the kinetic curves are linearized. A new wave must first be made and named in order to use the new wave name in the command window. This is done by clicking on Make Waves under the Data tab. In the Make Waves window, the name and number of rows can be entered. This wave can then be added to a table by selecting the wanted table, then clicking on Append Columns to Table under the Table tab. To linearize the data, the command window is used. In the command window the new wave is calculated as the linearized initial kinetic curve. This new wave is then plotted as a function of the time axis and fitted with lines. This is done the same as the

fitting of the initial kinetic curve, but selecting the line function in the Curve Fitting window.
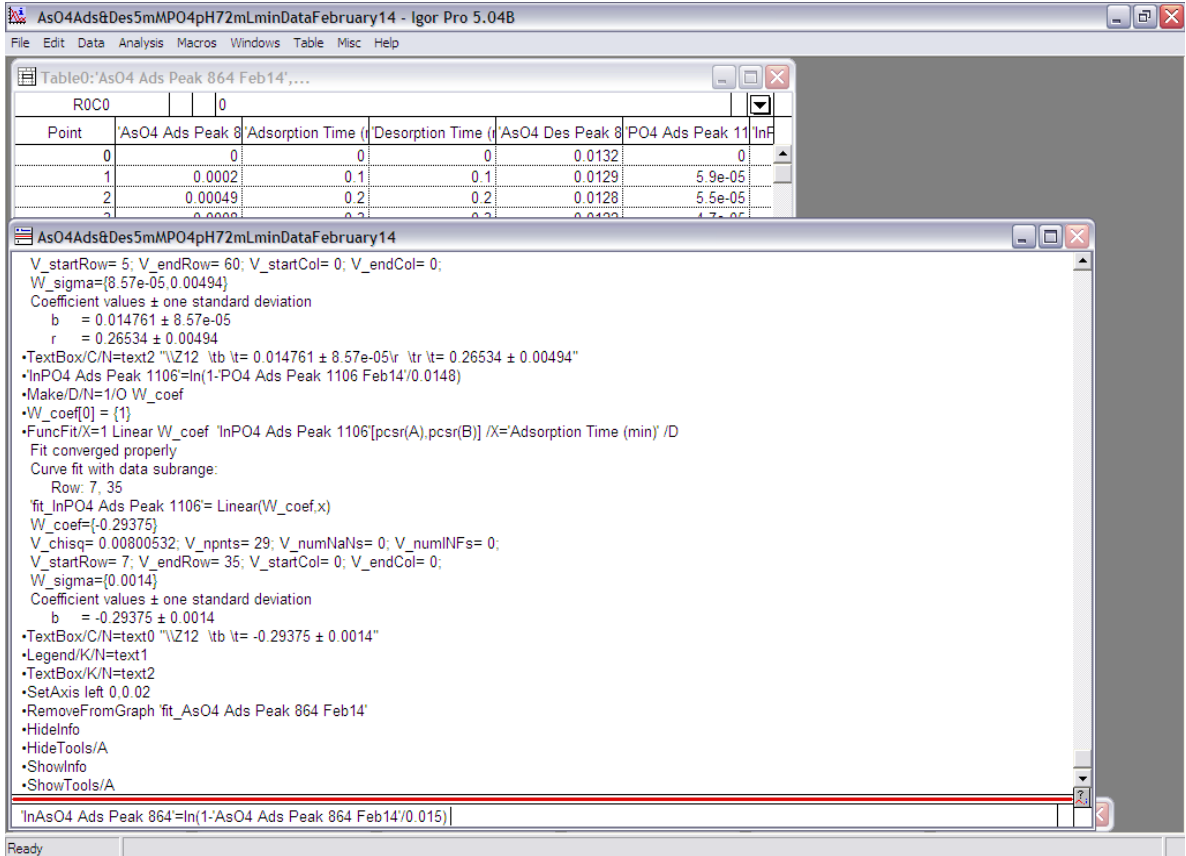
Figure C2. Command window in IGOR.

References:

1   Cullen, W.R. *Is Arsenic an Aphrodisiac? The Sociochemistry of an Element*; RSC Publishing: Cambridge, 2008

2   Mandal, B.K., Suzuki, T. K. Arsenic round the world: a review *Talanta.* 58 (2002) 201-235

3   Lollar, S.B. *Environmental Geochemistry*; Elsevier Ltd: Oxford, 2007

4   Brookins, D.G. Eh-pH diagrams for geochemistry *Spring. Ver.* 1988

5   Black, B.; Chin, D.T.; Perry, S.A.L. *Implementation of Arsenic Treatment Systems: Design Considerations, Operation, and Maintenance*; AWWA Research Foundation: 2002

6   Gomez-Caminero, A.; Howe, P.; Hughes, M.; Kenyon, E.; Lewis, D.R.; Moore, M.; Ng, J.; Aitio, A.; Becking, G. *Arsenic and Arsenic Compounds,* World Health Organization: Geneva, 2001

7   Bentley, R.; Chaateen, T.G. Microbial methylation of metalloids: arsenic, antimony, and bismuth *Microbio. Mol. Bio. Rev.* 66 (2002) 250-271

8   Hayakawa, T.; Kobayashi, Y.; Cui, X.; Hirano, S. A new metabolic pathway of arsenite: arsenic-glutathione complexes are substrates for human arsenic methyltransferase Cyt19 *Arch. Tox.* 79 (2005) 183-191

9   Paez-Espino D.; Tamames, J.; de Lorenzo, V.; Canovas, D. Microbial responses to environmental arsenic *Biomet.* 22 (2009) 117-130

10 Rosen, P. B. Biochemistry of arsenic detoxification *FEBS Letters* 529 (2002) 86-92

11 McLaughlin, M.J.; Parker, D.R.; Clarke, J.M. Metals and micronutrients – food safety issues *Field Crops Research* 60 (1999) 143-163

12 U.S. EPA: Arsenic Rule;http://www.epa.gov/safewater/arsenic/regulations.html.

13 Meharg, A.A.; Hartley-Whitaker, J. Arsenic uptake and metabolism in arsenic resistant and non-resistant plant species *New Phyt.* 154 (2005) 29-43

14 Kitchin, T.K. Recent advances in arsenic carcinogenesis: modes of action, animal model systems, and methylated arsenic metabolites *Toxicol. App. Pharm.* 172 (2001) 249-261

15 Alloway, B.J. *Heavy metals in soils* Chapman and Hall: Glasgow, 1995

16 Datta, R.; Sarkar, D.; Sharma, S.; Sand, K. Arsenic biogeochemistry and human health risk assessment in organo-arsenical pesticide-applied acidic and alkaline soils: an incubation study *Sci. Env.* 372 (2006) 39-48

17 Baernthaler, G.; Zischka, M.; Haraldsson, C.; Obernberger, I. Determination of major and minor ash-forming elements in solid biofuels *Biom. Bioen.* 30 (2006) 983-997

18 Fu, Q.; Argyropoulos, S.D.; Tilotta, C.D.; Lucia, A.L. Products and functional group distributions in pyrolysis oil of chromated copper arsenate (CCA)-treated wood, as elucidated by gas chromatography and a novel ^{31}P NMR-based method *Ind. Eng. Chem. Res.* 46 (2007) 5258-5264

19 Huang, J.H.; Ilgen, G.; Vogel, D.; Michalzik, B.; Hantsch, S.; Tennhardt, L.; Bilitewski, B. Emissions of inorganic and organic arsenic compounds via the leachate pathway from pretreated municipal waste materials: a landfill reactor study *Env. Sci.Tech.* 43 (2009) 7092-7097

20 Watts, M.J.; O'Reilly, J.; Marcilla, A.L.; Shaw, R.A.; Ward, N.I. Field based speciation of arsenic in UK and Argentinean water samples *Env. Geo. H.* 32 (2010) 479-490

21 Mestrot, A.; Feldmann, J.; Krupp, E.M.; Hossain, M.S.; Roman-Ross, G.; Meharg, A.A. Field fluxes and speciation of arsines emanating from soils *Env. Sci. Tech.* 45 (2011) 1798-1804

22 Bauer, M.; Fulda, B.; Blodau, C. Groundwater derived arsenic in high carbonate wetland soils: sources, sinks, and mobility *Sci. Env.* 401 (2008) 109-120

23 De Mello J.W.V.; Talbott, J.L.; Scott, J.; Roy, W.R.; Stucki, J.W. Arsenic speciation in arsenic-rich brazilian soils from gold mining sites under anaerobic incubation *Env. Sci. Pollut. Res.* 14 (2007) 388-396

24 Duester, L.; Diaz-Bone, R.A.; Kosters, J.; Hirner, A.V. Methylated arsenic, antimony and tin species in soils *J. Exp. Med.* 7 (2005) 1186-1193

25 Huang, J.H.; Matzner, E., Mobile arsenic species in unpolluted and polluted soils *Sci. Tot. Env.* 377 (2007) 308-318

26 Geiszinger, A.; Goessler, W.; Kosmus, W. Organoarsenic compounds in plants and soil on top of an ore vein *Appl. Organometal. Chem.* 16 (2002) 245-249

27 Huang, J.H.; Matzner, E. Dynamics of organic and inorganic arsenic in the solution phase of an acidic fen in Germany *Elsevier* 70 (2006) 2023-2033

28 Zhao, R.; Zhao, M.; Wang, H.; Taneike, Y.; Zhang, X. Arsenic speciation in moso bamboo shott – a terrestrial plant that contains organoarsenic species *Sci. Tot. Env.* 371 (2006) 293-303

29 Huang, J.H.; Matzner, E. Biogeochemistry of organic and inorganic arsenic species in a forested catchment in Germany *Environ. Sci. Technol.* 41 (2007) 1564-1569

30 Zagury, J.G. Inorganic arsenic speciation in soil and groundwater near in-service chromated copper arsenate-treated wood poles *Env. Tox. Chem.* 27 (2008) 799-807

31 Chappell, J.; Chiswell, B.; Olszowy, H. Speciation of arsenic in a contaminated soil by solvent extraction *Talansa* 42 (1995) 323-329

32 Rossman, G.T. Mechanism of arsenic carcinogenesis: an integrated approach *Mutat. Res.* 533 (2003) 37-65

33 Thomas, J.D.; Styblo, M.; Lin, S. The cellular metabolism and systemic toxicity of arsenic *Tox. App. Pharm.* 176 (2001) 127-144

34 Hirano, S.; Kobayashi, Y.; Cui, X.; Kanno, S.; Hayakawa, T.; Shraim, A. The accumulation and toxicity of methylated arsenicals in endothelial cells: important roles of thiol compounds *Toxicol. App. Pharm.* 198 (2004) 458-467

35 Ochi, T.; Kaise, T.; Oya Ohta, Y. Glutathione plays different roles in the induction of the cytotoxic effects of inorganic and organic arsenic compounds in cultured BALB/c 3T3 cells *Experientia* 50 (1994) 115-120

36 Eguchi, N.; Kuroda, K.; Endo, G. Metabolites of arsenic induced tetraploids and mitotic arrest in cultured cells *Arch. Environ. Contam. Toxicol.* 32 (1997) 141-145

37 Shiobara, Y.; Ogra, Y.; Suzuki, K.T. Animal species difference in the uptake of dimethylarsinous acid (DMA(III)) by red blood cells *Chem. Res. Toxicol.* 14 (2001) 1446-1452

38 Nesnow, S.; Roop, B.C.; Lambert, G.; Kadiiska, M.; Mason, R.P.; Cullen, W.R.; Mass, M.J. DNA damage induced by methylated trivalent arsenicals is mediated by reactive oxygen species *Chem. Res. Toxicol.* 15 (2002) 1627-1634

39 Suzuki, K.T. Glutathione-conjugated arsenics in the potential hepato-enteric circulation in rats *Chem. Res. Toxicol.* 14 (2001) 1604-1611

40 Yamanaka, K.; Okada, S. Induction of lung-specific DNA-damage by metabolically methylated arsenics via the production of free-radicals *Environ. Health Perspect.* 102 (1994) 37-40

41 Hirano, S.; Furuyama, A.; Koike, E.; Kobayashi, T. Oxidative-stress potency of organic extracts of diesel exhaust and urban fine particles in rat heart microvessel endothelial cells *Toxicology* 187 (2003) 305-312

42 Salnikow, K.; Zhitkovich, A. Genetic and epigenetic mechanisms in metal carcinogenesis and cocarcinogenesis: nickel, arsenic, and chromium *Chem. Res. Toxicol.* 21 (2008) 28-44

43 Kenyon, E. M.; Hughes, M. F. A concise review of the toxicity and carcinogenicity of dimethylarsinic acid *Tox.* 160 (2001) 227-236

44 Brown, J.L.; Kitchin, K.T.; George, M. Dimethylarsinic acid treatment alters six different rat biochemical parameters: relevance to arsenic carcinogenesis *Teratogen. Carcinogen. Mutagen.* 17 (1997) 71-84

45 Catalano, J. G.; Park, C.; Fenter, P.; Zhang, Z. Simultaneous inner- and outer-sphere arsenate adsorption on corundum and hematite *Geochim. Cosmochi. Acta* 72 (2008) 1986-2004

46 Adamescu, A.; Mitchell, W.; Hamilton, I.P.; Al-Abadleh, H.A. Insights into the surface complexation of dimethylarsinic acid on iron (oxyhydr)oxides from ATR-FTIR studies and quantum chemical calculations *Env. Sci. Tech.* 44.20 (2010) 7802-7

47 Mitchell, W.; Goldberg, S.; Al-Abadleh, H. A. In-situ ATR-FTIR and surface complexation modeling studies on the adsorption of dimethylarsinic acid and p-arsanilic acid on iron-(oxyhydr)oxides *J. Coll. Int. Sci.* 358 (2011) 534-540

48 Adamescu, A.; Hamilton, I.P.; Al-Abadleh, H.A. Thermodynamics of dimethylarsinic acid and arsenate interactions with hydrated iron-(oxyhydr)oxide clusters: DFT calculations *Env. Sci. Tech.* 45 (2011) 10438-10444

49 Carabante, I.; Grahn, M.; Holmgren, A.; Kumpiene, J.; Hedlund, J. Adsorption of as (V) on iron oxide nanoparticle films studied by in situ ATR-FTIR spectroscopy *Coll. Surf. A* 346.1-3 (2009) 106-13

50 Cox. C.D.; Ghosh, M.M. Surface complexation of methylated arsenates by hydrous oxides *Wat. Res.* 28 (1994) 1181-1188

51 Martin, M.; Celi, L.; Barberis, E.; Violante, A.; Kozak, L.M.; Huang, P.M. Effect of humic acid coating on arsenic adsorption on ferrihydrite-kaolinite mixed systems *Can. J. Soil Sci.* 89 (2009) 421-434

52 Luxton, P.T.; Eick, J.M.; Scheckel, G.K. Arsenate adsorption on ruthenium oxides: a spectroscopic and kinetic investigation *J. Coll. Int. Sci.* 325 (2008) 23-30

53 Bowell, R.J. Sorption of arsenic by iron oxides and oxyhydroxides in soils *App. Geochem.* 9 (1994) 279-286

54 Gupta, S.S.; Bhattacharyya, G.K. Adsorption of heavy metals on kaolinite and montmorillonite: a review *Phys. Chem. Chem. Phys.* 14 (2012) 6698-6723

55 Chabot, M.; Tuan H.; Al-Abadleh, H.A. ATR-FTIR studies on the nature of surface complexes and desorption efficiency of p-arsanilic acid on iron (oxyhydr)oxides *Env. Sci.Tech.* 43.9 (2009) 3142-7

56 Depalma, S.; Cowen, S.; Hoang, T.; Al-Abadleh, H.A. Adsorption thermodynamics of p-arsanilic acid on iron (oxyhydr)oxides: in-situ ATR-FTIR studies." *Env. Sci. Tech.* 42.6 (2008) 1922-7

57 Gimenez, J.; Martinez, M.; de Pablo, J.; Rovira, M.; Duro, L. Arsenic sorption onto natural hematite, magnetite, and goethite *J Haz Mat* 141 (2007) 575-580

58 Shimizu, M.; Arai, Y.; Sparks, D.L. Multiscale assessment of methylarsenic reactivity in soil. 1. Sorption and desorption on soils *Env. Sci. Tech.* 45 (2011) 4293-4299

59 Lafferty, B.J.; Loeppert, R.H. Methyl arsenic adsorption and desorption behaviour on iron oxides *Env. Sci. Tech.* 39 (2005) 2120-2127

60 Tofan-Lazar, J.; Al-Abadleh H.A. ATR-FTIR studies on the adsorption/desorption kinetics of dimethylarsinic acid on iron-(oxyhydr)oxides. *J. Phys. Chem. A* 116 (2012) 1596-1604

61 Pigna, M.; Krishnamurti, G. S. R.; Violante, A. Kinetics of arsenate sorption-desorption from metal oxides: effects of residence time *Soil Sci. Soc. Am. J.* 70 (2006) 2017-2027

62 Puccia, V.; Luengo, C.; Avena, M. Phosphate desorption kinetics from goethite as induced by arsenate *Coll. Surf. A* 348 (2009) 221-227

63 Strauss R.; Brummer, G.W.; Barrow, N.J. Effects of crystallinity of goethite: II. Rates of sorption and desorption of phosphate *Euro. J. Soil Sci.* 48 (1997) 101-114

64 O'Reilly, S. E.; Strawn, D. G.; Sparks, D. L. Residence time effects of arsenate adsorption/desorption mechanisms on goethite *Soil Sci. Soc. Am. J.* 65 (2001) 67-77

65 Zhang, J.; Stanforth, R. Slow adsorption reaction between arsenic species and goethite (α-FeOOH): diffusion or heterogeneous surface reaction control *Langmuir* 21 (2005): 2895-2901

66 Frau, F.; Addari, D.; Atzei, D.; Biddau, R.; Cidu, R.; Rossi, A. Influence of major anions on As(V) adsorption by synthetic 2-line ferrihydrite. Kinetic investigation and XPR study of the competitive effect of bicarbonate *Water Air Soil Pollut* 205 (2010) 25-41

67 Ho, Y.S.; McKay, G. A comparison of chemisorption kinetic models applied to pollutant removal on various sorbents *Trans IChemE* 76 (1998) 332-341

68 Xu, R.K.; Yu, G.; Kozak, L.M.; Huang, P.M. Desorption kinetics of arsenate adsorbed on Al(oxy)hydroxides formed under the influence of tannic acid *Geoderma* 148 (2008) 55-62

69 Antelo, J. Analysis of phosphate adsorption onto ferrihydrite using the CD-MUSIC model *J Coll. Int. Sci.* 347 (2010) 112-119

70 Jing, C.; Meng, X.; Liu, S.; Baidas, S.; Patraju, R.; Christodoulatos, C.; Korfiatis, G.P. Surface Complexation of organic arsenic on nanocrystalline titanium oxide *J. Coll. Int. Sci.* 290 (2005) 14-21

71 Shimizu, M.; Ginder-Vogel, M.; Parikh, S.J.; Sparks, D.L. Molecular scale assessment of methylarsenic sorption on aluminum oxide *Env. Sci.Tech.* 44 (2010) 612-617

72 Loring, J.S.; Sandstrom, M.H.; Noren, K.; Persson, P. Rethinking arsenate coordination at the surface of goethite *Chem. Eur. J.* 15 (2009) 5063-5072

73 Grossl, P. R.; Eick, M.; Sparks, D.L.; Goldberg, S.; Ainsworth, C.C. 1.Arsenate and chromate retention mechanisms on goethite. 2.Kinetic evaluation using a pressure-jump relaxation technique *Env. Sci. Tech.* 31 (1997) 321-326

74 Goldberg, S.; Johnston, C.T. Mechanisms of arsenic adsorption on amorphous oxides evaluated using macroscopic measurements, vibrational spectroscopy, and surface complexation modeling *J. Coll. Int. Sci.* 234 (2001) 204-216

75 Elzinga, E.J.; Sparks, D.L. Phosphate adsorption onto hematite: An in situ ATR-FTIR investigation of the effects of pH and loading level on the mode of phosphate surface complex. *J. Coll.Inter.Sci.* 308 (2007) 53-70

76 Adamescu, A.; Gray, H.; Stewart, K.M.E.; Hamilton, I.P.; Al-Abadleh, H.A. Trends in the frequencies of $\nu(AsO_xH_{x-1})$ [x = 2-4] in selected As(V)-containing compounds investigated using quantum chemical calculations *Can. J. Chem.* 88 (2010) 65-77

77 Kubicki, J.D.; Kwon, K.D.; Paul, K.W.; Sparks, D.L. Surface complex structures modelled with quantum chemical calculations: carbonate, phosphate, sulphate, arsenate and arsenite *Europ. J. Soil Sci.* 58 (2007) 932-944

78 Arai, Y.; Sparks, D.L. ATR-FTIR spectroscopic investigation on phosphate adsorption mechanisms at the ferrihydrite-water interface *J. Coll. Inter. Sci.* 241 (2001) 317-326

79 Grossl, P.R.; Sparks, D.L., Rapid kinetics of Cu(II) adsorption/desorption on goethite *Envi. Sci. Tech.* 28 (1994) 1422-1429

80 Persson, P.; Nilsson, N.; Sjoberg, S. Structure and bonding of orthophosphate ions at the iron oxide aqueous interface *J. Coll. Inter. Sci.* 177 (1996) 263-275

81 Myneni, S.C.B.; Traina, S.J.; Waychunas, G.A.; Logan, T.J. Experimental and theoretical vibrational spectroscopic evaluation of arsenate coordination in aqueous solutions, solids and at the mineral-water interfaces *Geochim. Cosmochim. Acta* 62 (1998) 3285-3300

82 Luengo, C.; Brigante, M.; Antelo, J.; Avena, M. Kinetics of phosphate adsorption on goethite: comparing batch adsorption and ATR-IR measurements *J. Coll. Int. Sci.* 300 (2006) 511-518

83 Parikh, S.J.; Lafferty, B.J.; Sparks, D.L. An ATR-FTIR spectroscopic approach for measuring rapid kinetics at the mineral/water interface *J. Coll. Int. Sci.* 320 (2008) 177-185

84 Lakshmipathiraj, P.; Narasimhan, B.R.V.; Prabhakar, S.; Raju, G.B. Adsorption of arsenate on synthetic goethite from aqueous solutions *J. Haz. Mat. B* 136 (2006) 281-287

85 Luengo, C.; Brigante, M.; Avena, M. Adsorption kinetics of phosphate and arsenate on goethite. A comparative study *J. Coll. Int. Sci.* 311 (2007) 354-360

86 Roddick-Lanzilotta, A.J.; McQuillan, A.J.; Craw, D. Infrared spectroscopic characterization of arsenate(V) ion adsorption from mine waters, Macraes mine, New Zealand *Appl. Geochem.* 17 (2002) 445-454

87 Cowen S.; Duggal, M.; Hoang, T.; Al-Abadleh, H.A. Vibrational spectroscopic characterization of some environmentally important organoarsenicals – a guide for understanding the nature of their surface complexes *Can. J. Chem.* 86 (2008) 942-950

88 Sadiq, M. Arsenic chemistry in soils: an overview of thermodynamic predictions and field observations *Water Air Soil Pollut* 93 (1997) 117-136

89 Chen, B.; Stein, A.F.; Castell, N.; de la Rosa, J.D.; Sanchez de la Campa, A.M.; Gonzalez-Castanedo, Y.; Draxler, R.R. Modeling and surface observations of arsenic dispersion from a large Cu-smelter and southwestern Europe *Atmos. Env.* 49 (2012) 114-122